Strategic Phase Modulation in $Na_{0.8}(Mn\text{-}Fe\text{-}Ni)O_2$ System Delivers High Energy Density and Structural Stability

Samriddhi Saxena [a], Hari Narayanan Vasavan [a], Neha Dagar [a], Velaga Srihari [b], Asish Kumar Das [a], Pratiksha Gami [a], Sonia Deswal [c], Pradeep Kumar [c], Himanshu Kumar Poswal [b], Sunil Kumar [a,*]

[a] *Department of Metallurgical Engineering and Materials Science, Indian Institute of Technology Indore, Simrol, 453552, India*

[b] *High Pressure & Synchrotron Radiation Physics Division, Bhabha Atomic Research Centre, Mumbai 400085, India*

[c] *School of Physical Sciences, Indian Institute of Technology Mandi, Mandi, 175005, India*

[*] *E-mail: sunil@iiti.ac.in*

ABSTRACT

The growing demand for sustainable energy storage positions Na-ion batteries as a compelling, cost-effective alternative to Li-ion technology. This study investigates the impact of phase engineering on structural and electrochemical behavior in the $Na_{0.8}(Mn\text{-}Fe\text{-}Ni)O_2$ system, harnessing the outstanding performance characteristics of layered oxide cathodes. Samples calcined at 700 °C, 800 °C, 900 °C, and 1000 °C display diverse phase compositions, including P and O-type phases. Rietveld refinement of X-ray Diffraction (XRD) data shows that increasing Ni content resulted in reduced Na-O layer spacings, compromising rate performance. P2/O3-$Na_{0.8}Mn_{0.53}Fe_{0.14}Ni_{0.33}O_2$, calcined at 900 °C, achieved highest discharge capacity (~139 mAh g^{-1}), followed by $Na_{0.8}Mn_{0.53}Fe_{0.25}Ni_{0.22}O_2$, calcined at 800 °C(~134 mAh g^{-1}) at 0.1C. For constant Fe content, decreasing the Ni/Mn ratio results in sloping charge-discharge curves, indicating reduced honeycomb ordering during cycling. P2 phases formed at 1000 °C show significant capacity retention loss. $Na_{0.8}Mn_{0.64}Fe_{0.14}Ni_{0.22}O_2$ demonstrates the best overall performance, retaining over 88% of its initial capacity after 50 cycles at 0.2C. *Operando* Synchrotron XRD analysis reveals a minimal (~-1.6%) change in the *c* parameter during cycling, correlating with exceptional capacity retention. This work emphasizes the critical role of phase composition, metal ratios, and synthesis temperature in optimizing $Na_{0.8}(Mn\text{-}Fe\text{-}Ni)O_2$ based cathodes for high-performance Na-ion batteries.

KEYWORDS: *Na-ion batteries, layered oxides, Mn-Fe-Ni system, electrochemical performance, operando Synchrotron XRD*

1. INTRODUCTION

The growing demand for sustainable and cost-effective energy storage solutions has generated significant interest in sodium-ion batteries (SIBs) as a viable alternative to lithium-ion batteries (LIBs). Na, being more abundant and widely distributed than Li, offers an economical and environmentally friendly solution for energy storage applications [1, 2]. However, developing high-performance cathode materials remains a critical challenge for SIBs in achieving adequate energy densities, cycling stability, and rate capabilities [3]. Various cathode materials have been explored for SIBs, such as polyanionic compounds ($Na_3V_2(PO_4)_3$), which provide excellent structural stability and high operating voltages, though their capacity remains limited [4, 5]. Layered transition metal (TM) oxides (Na_xTMO2) are promising for SIBs, offering high capacity, structural flexibility, and tunable electrochemical properties [6, 7].

Layered oxides exhibit three main structures, P2, P3, and O3, which differ in sodium-ion coordination and stacking sequence [8, 9]. The P2 and the P3 phases, with prismatic sites for sodium-ion, offer excellent sodium-ion mobility, superior rate performance, and cycling stability [10-13]. Yet, they may experience capacity degradation at high voltages due to structural transformations [14]. The O3 phase, with octahedral sodium-ion coordination, offers higher theoretical capacities but suffers from slower sodium-ion diffusion, limiting its rate performance [15, 16]. Various strategies have been proposed to improve the electrochemical performance of these phases, such as preparing multi-transition metal systems [17, 18], creating multiphasic systems [19-21], and surface modification [22, 23].

Single TM layered oxides are attractive cathode materials for SIBs due to their compositional simplicity and high theoretical capacities. Even though manganese-based layered oxides (Na_xMnO_2) can deliver discharge capacities up to 185 mAh g^{-1}, their practical application is limited by the Jahn–Teller effect of Mn^{3+}, which induces structural distortions, reduces sodium-ion diffusivity, and degrades cycling performance, as well as the low potential of the Mn^{3+}/Mn^{4+} redox couple, which reduces the cell voltage and overall energy density. Additionally, phase transitions compromise their electrochemical stability [24-26]. Similarly, iron-based layered oxides (Na_xFeO_2) are valued for their abundance, low toxicity, and environmental sustainability [27, 28]. However, they face significant challenges, including severe phase transitions during cycling, poor rate capability, and high sensitivity to air and moisture, which accelerate structural degradation and hinder long-term performance [28-30].

To overcome the limitations of single TM layered oxides, binary transition metal layered oxides have been developed to enhance both structural stability and electrochemical performance. For instance, P2-$Na_{2/3}Fe_{1/2}Mn_{1/2}O_2$ demonstrates a promising discharge capacity of 190 mAh g^{-1} within a voltage range of 1.5 – 4.3 V. But, this material experiences a phase transition to the OP4 structure when charged beyond 4.2 V, leading to compromised cycling stability [31, 32]. The high capacity is attributed to the Mn^{3+}/Mn^{4+} and Fe^{3+}/Fe^{4+} redox couples, though issues such as sensitivity to air and phase instability remain [33]. Likewise, the extensively studied P2-$Na_{2/3}Ni_{1/3}Mn_{2/3}O_2$ delivers a reversible capacity of 160 mAh g^{-1} in the 2.0 – 4.5 V range, but charging beyond 4.2 V leads to an irreversible P2 to O2 phase transition, resulting in a significant volume change and reduced capacity retention [34-37]. While O3-type $NaNi_{1/2}Mn_{1/2}O_2$ achieves a higher reversible capacity of 200 mAh g^{-1} within the 2.2 – 4.5 V range, the practical capacity is limited to 120 mAh g^{-1} in the narrower voltage range of 2.2 – 3.8 V [38]. Despite the enhanced electrochemical performance, these binary transition metal oxides face challenges related to multi-step charge-discharge behavior, which affects their long-term cyclability [39].

Ternary transition metal systems provide a promising alternative, offering solid solution zones through strategic elemental combinations. This approach addresses the limitations of binary systems and enhances electrochemical performance. Layered oxides incorporating Mn, Fe, and Ni are particularly attractive due to their synergistic properties. Mn and Fe, being abundant, reduce costs, while the Ni redox couple's two-electron transfer boosts capacity. Moreover, the presence of Ni and Fe contributes to a higher nominal voltage, improving energy density. For example, $NaFe_{1/3}Ni_{1/3}Mn_{1/3}O_2$ is the most extensively studied material within the Na(Mn-Fe-Ni)O_2 system, delivering a specific capacity of 130 mAh g^{-1} and ~85% capacity retention after 100 cycles [40-43]. Another representative P2-type $Na_{2/3}Fe_{1/3}Ni_{1/3}Mn_{1/3}O_2$ material in the ternary system of Mn-Fe-Ni transition metals displays a specific capacity of 100 mAh g^{-1} and ~75% capacity retention after 60 cycles in the 2.0 – 4.2 V range [44]. Several other cathodes in the Mn-Fe-Ni pseudo ternary system have been explored, such as $NaMn_{0.5}Ni_{0.3}Fe_{0.1}Mg_{0.1}O_2$ [45], $Na_{0.67}Ni_{0.1}Fe_{0.1}Mn_{0.8}O_2$ [46], $Na_{0.6}Ni_{0.22}Fe_{0.11}Mn_{0.66}O_2$ [7], $Na_{0.9}Ni_{0.35}Fe_{0.2}Mn_{0.45}O_2$ [47], $Na_{0.76}Mn_{0.5}Ni_{0.3}Fe_{0.1}Mg_{0.1}O_2$ [45], $Na_{0.67}Ni_{0.15}Fe_{0.35}Mn_{0.5}O_2$ [48]. Additionally, biphasic systems with P2/O3, P2/P3, and ternary phase combinations promise high-voltage stability and prolonged cycle life [21, 49, 50]. Despite numerous studies, optimization of the metal ratios and understanding the influence of calcination temperatures on phase evolution is crucial for unlocking the full potential of these ternary systems. This study focuses on the phase composition, structural characteristics, and electrochemical performance of $Na_{0.8}$(Mn-Fe-

Ni)O_2 cathodes selected from a pseudo ternary diagram (Fig. 1) and synthesized at different calcination temperatures (700 °C, 800 °C, 900 °C, and 1000 °C). The research emphasizes the role of phase fractions, transition metal ratios, and lattice parameters in determining the material's performance.

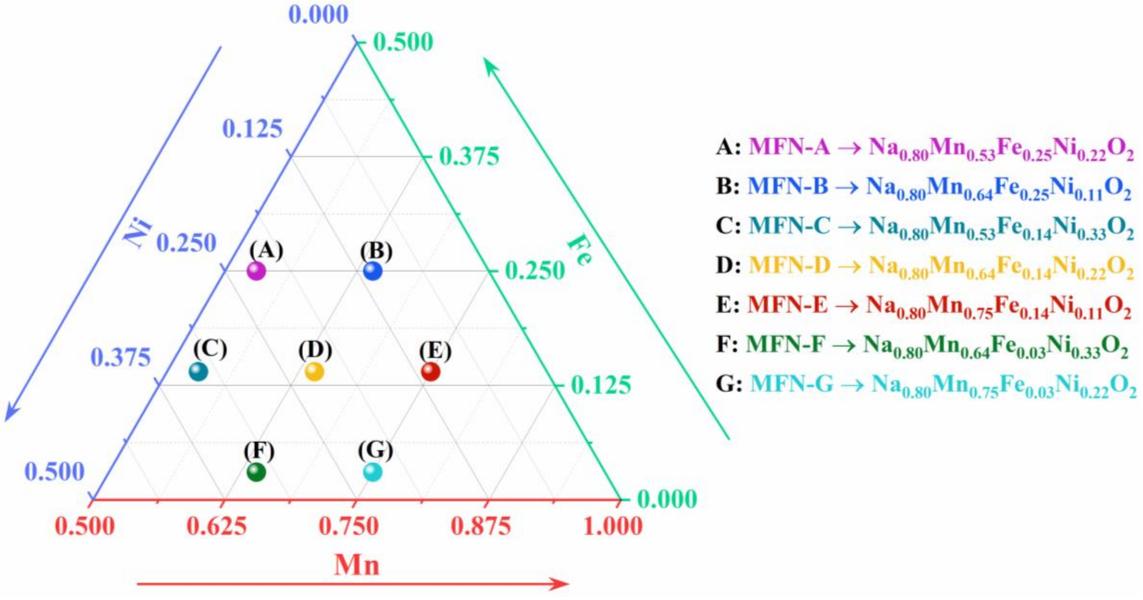

Fig. 1. Compositions in the $Na_{0.8}$(Mn-Fe-Ni)O_2 pseudo-ternary system and their abbreviations studied in this work.

The primary objective of this work is to identify compositions within the $Na_{0.8}$(Mn-Fe-Ni)O_2 (MFN) system that exhibit a stable structure, high nominal voltage to enhance energy density, and minimal capacity fading upon cycling. Although numerous studies have investigated the effects of varying Mn and Ni transition metals on the structural and electrochemical properties of layered oxides, this study specifically explores the influence of the Mn/Ni ratio while maintaining a constant Fe content. To examine the impact of the Ni/Mn ratio on the structural and electrochemical properties, additional characterization was conducted on MFN-C, MFN-D, and MFN-E, all synthesized at 800 °C. MFN-D showed superior performance across all calcination temperatures, retaining over 88% of its initial capacity after 50 cycles. Advanced characterization techniques, such as *operando* Synchrotron studies, correlate structural properties and strain to electrochemical stability. These findings provide critical insights into the design of high-performance cathode materials and the advancement of sodium-ion battery technology.

2. MATERIALS AND METHODS

All compositions within the pseudo-ternary $Na_{0.8}$(Mn-Fe-Ni)O_2 diagram were synthesized using a sol-gel method. Na_2CO_3 (SRL, 99.9%), $C_4H_6MnO_4 \cdot 4H_2O$ (Sigma-Aldrich, >99%), $Fe(NO_3)_3 \cdot 9H_2O$ (Rankem. 98%), and $C_4H_6NiO_4 \cdot 4H_2O$ (Sigma-Aldrich, 98%) were measured in stoichiometric amounts and mixed in deionized water. This mixture was stirred for 8 hours, followed by the addition of citric acid ($C_6H_8O_7$) as a chelating agent and ethylene glycol ($C_2H_6O_2$) as a gelling agent. The resulting solution was continuously stirred to form a homogeneous mixture, which was then heated to form a gel. The gel was dried and subsequently subjected to heat treatment at 550 °C, followed by calcination at 700 °C, 800 °C, 900 °C, and 1000 °C in a muffle furnace under ambient air. After calcination, the products were allowed to cool naturally and then transferred to an argon-filled glove box to prevent moisture contact from the air.

Phase identification was performed by X-ray Diffraction (XRD) using an Empyrean instrument from Malvern Panalytical with Cu-Kα radiation. The XRD data were collected over a 2θ range of 10-70° with a step size of 0.01° and analyzed using Rietveld refinement with Topas academic software (version 6) [51]. Morphological studies of the samples were conducted using field emission scanning electron microscopy (FESEM) with a JEOL-7610 model. Energy dispersive X-ray spectroscopy (EDS) was employed to investigate the elemental distribution within the samples. X-ray photoelectron spectroscopy (XPS) using a Thermo Fisher Scientific instrument with a 1486.6 eV (Al Kα) X-ray source was utilized to determine the oxidation states of elements in the cathode materials.

The positive electrodes were prepared by coating a slurry composed of 75% active material, 10% Ketjen black, and 15% polyvinylidene fluoride (PVDF) binder in N-methyl-2-pyrrolidone (NMP) solvent. This slurry was coated to an aluminum (Al) current collector, dried under vacuum, and then punched into 14 mm discs to achieve an active material loading of 3-4 mg cm^{-2} and an apparent active mass density of ~ 1.5-2.0 g cm^{-3}. CR2032 coin cells were assembled in an argon-filled glove box, using the prepared electrodes along with sodium metal as the negative electrode. The electrolyte used was 1M $NaClO_4$ in a 1:1 mixture of ethylene carbonate (EC) and propylene carbonate (PC), with Whatman GF/D as the separator. Galvanostatic charge-discharge (GCD) experiments were conducted at various current densities using a Neware battery tester (Model CT-4008T). The same equipment was used to perform the galvanostatic intermittent titration technique (GITT) and calculate the diffusion coefficient of Na-ions in the cathode material. The phase transformations that occurred during electrochemical cycling were investigated by operando studies carried out using extreme conditions-angle dispersive/energy dispersive synchrotron X-ray diffraction (Beamline 11) at Indus-2 beamline Raja Ramanna Centre for Advanced Technology (RRCAT) with a beam wavelength of 0.7313 Å and beam energy of 2.5 GeV. The coin cells for the operando studies were prepared by drilling 3 mm holes in the CR2032 coin-cell casing to allow the beam to pass through the cell. A Kapton tape was used to cover the drilled holes in coin cell casings to prevent environmental exposure.

3. RESULTS AND DISCUSSION

3.1. Structural characterization

3.1.1. X-ray diffraction

To investigate the temperature-dependent phase behavior of selected compositions in the $Na_{0.8}(Mn\text{-}Fe\text{-}Ni)O_2$ system, the samples were calcined at four temperatures – 700 °C, 800 °C, 900 °C, and 1000°C - resulting in varying amounts of the P2, P3, and O3 phases (Fig. 2). Table S1 (Supplementary material) summarizes the phase fractions obtained for all compositions at different calcination temperatures. The fractions of various phases present in each sample were quantified through Rietveld refinement of XRD data. The XRD results in Figs. S1-S4 revealed that all peaks corresponded to the Bragg positions of the O3, P3, and P2 phases, except for MFN-C calcined at 1000 °C, which contained trace amounts of NiO. The P3 phase was observed in all samples calcined at 700 °C, which aligns with previous studies showing that lower calcination temperatures favor P3 phase formation [52-54].

Moreover, compositions with a higher Fe/Mn ratio have a higher tendency to form the O3 phase, consistent with earlier reports [13]. There is also a noticeable correlation between Mn content and phase composition. As the Mn content increases, the samples show a mix of P2 and P3 phases, with trace amounts of O3. This can be explained by the lower electronegativity of Mn (1.55 on the Pauling scale) compared to Fe (1.83) and Ni (1.91), which increases the repulsion between oxygen ions and promotes the formation of prismatic sites over octahedral sites.

The phase diagram at 800 °C (Fig. 2(b)) indicates that the P2 phase becomes more stable as the calcination temperature increases, supporting previous studies [13]. The transition from P3 to P2 requires the breaking of TM─O bonds, which necessitates sufficiently high temperatures. A correlation between phase structure and Ni content was also observed, with a Ni content of 0.33 favoring the formation of the P3 and O3 phases alongside the dominant P2 phase at 800 °C. On increasing the calcination temperature to 900 °C and 1000 °C, the P2 phase becomes dominant, although trace amounts of the O3 phase persist in some low-Mn compositions. This is due to the Na content being 0.8, which is near the threshold for stabilizing low-Na O3 phases. This analysis indicates that the phase stability in these systems is highly dependent on the careful balance of Fe, Mn, and Ni content, with different phases favored under specific compositional and temperature conditions.

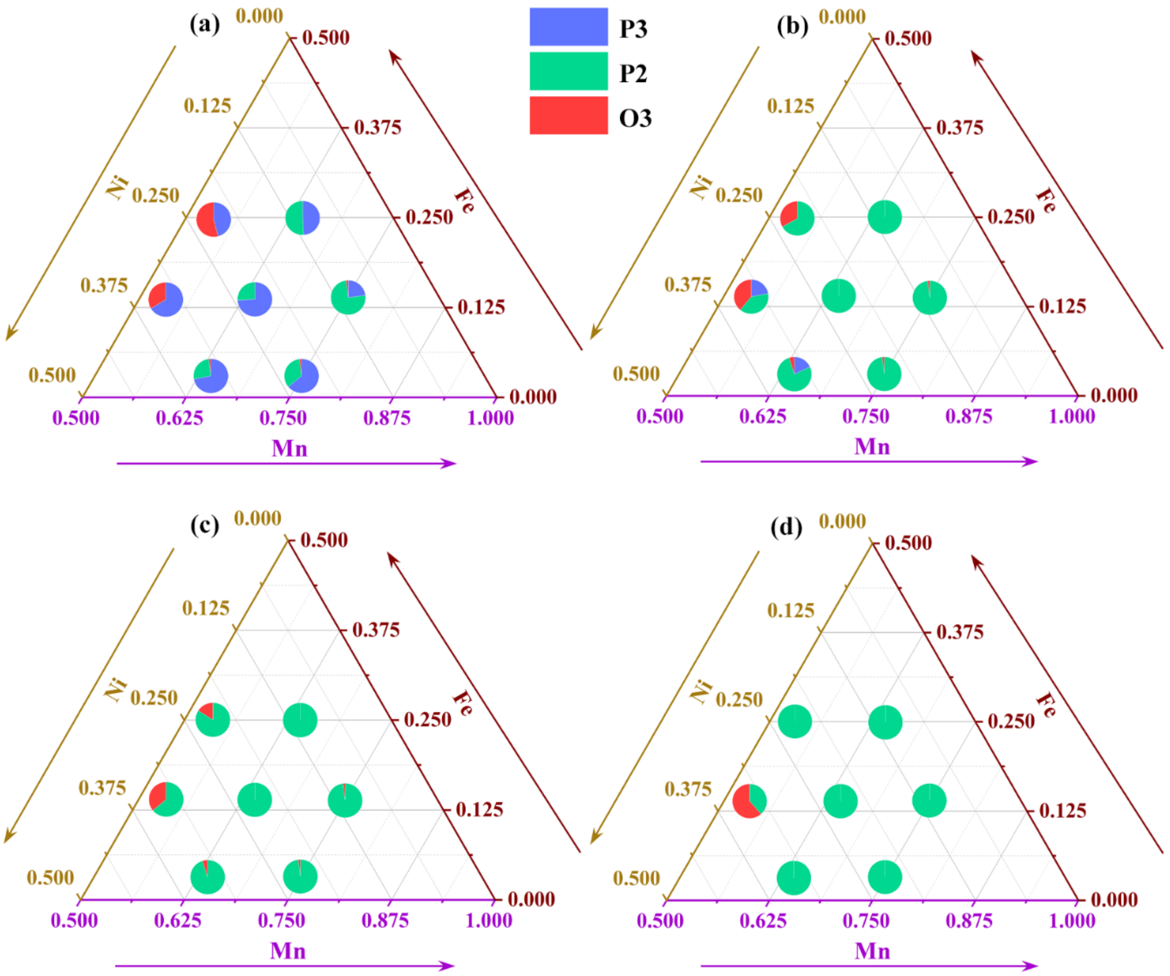

Fig. 2. Fractions of the P3, P2, and O3 phases in MFN samples calcined at (a) 700 °C, (b) 800 °C, (c) 900 °C, and (d) 1000 °C.

The Rietveld refinement of the XRD data shows that the P2, P3, and O3 phases correspond to the $P6_3/mmc$, $R3m$, and $R\bar{3}m$ space groups, respectively (Figs. 3, S5-S7). The refined lattice parameters are detailed in Tables S2–S5. The evolution of the *c* parameter in the $Na_{0.8}$(Mn-Fe-Ni)O_2 system is primarily influenced by the concentrations of Mn, Ni, and Fe, with each element contributing uniquely to the structure at different calcination temperatures.

At 800 °C, the *c* parameter shows straightforward trends. An increase in Ni content results in a consistent decrease in the *c* parameter, which is contrary to the expected increase, given that the ionic radius of Ni^{2+} in six-coordination (0.69 Å) is larger than that of Mn^{3+} (0.58 Å), Mn^{4+} (0.53 Å), and Fe^{3+} (0.55 Å). Along the constant Ni lines, an increase in the Mn/Fe ratio leads to a corresponding increase in the *c* parameter. This suggests that the effects of the higher electronegativity of transition metal ions on the lattice parameters are more significant than the effects of larger ionic radii in these samples.

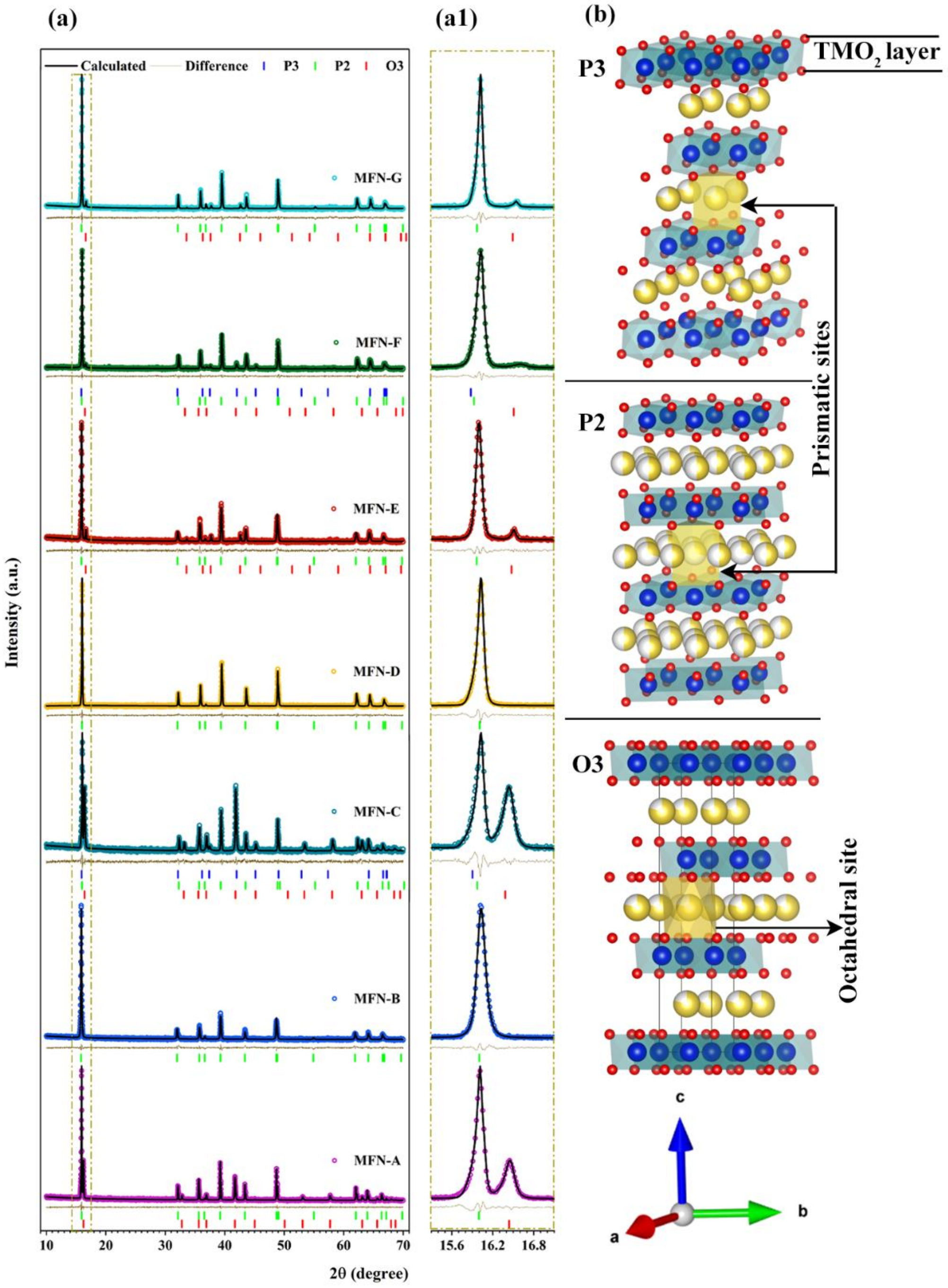

Fig. 3. (a) Rietveld refined patterns of MFN samples calcined at 800 °C, (a1) Magnified view of the most intense peak of P3, P2, and O3 phases. (b) Schematic of P3, P2, and O3 crystal structure.

At 700 °C, the *c* parameter exhibits complex behavior with varying Ni content. The *c* parameter first increases and then decreases as Ni content decreases. At 900 °C, the influence of transition metals is more complex. Decreasing Ni content results in an increase in the *c* parameter, but along constant Ni lines, increasing the Mn/Fe ratio reduces it. At 1000 °C, as Ni content decreases, the *c* parameter consistently increases. For constant Ni, the *c* parameter increases with a rise in the Mn/Fe ratio.

Overall, the lattice parameter behavior of the $Na_{0.8}(Mn\text{-}Fe\text{-}Ni)O_2$ system is highly dependent on the interplay between Fe, Mn, and Ni content, with the *c* parameter demonstrating distinct variations influenced by compositional changes at each calcination temperature. Mn generally promotes an increase in the *c* parameter, while the influence of Fe and Ni depends more on their relative concentrations and the overall temperature, indicating a complex dependence of lattice parameters on transition metal ratios in this layered oxide system. Detailed refinement parameters for all samples are provided in Tables S6-S33 (Supplementary material).

3.1.2. Scanning electron microscopy

The morphology of MFN-C, MFN-D, and MFN-E samples on the constant Fe line was analyzed using FESEM, and the corresponding SEM micrographs are presented in Figs. 4, S8, and S9. The images reveal that the particles exhibit a flat, plate-like morphology. While the average particle size ranges between 1.5 µm and 1.8 µm, MFN-C displays a broader distribution, with particles varying from 0.5 to 2.4 µm. Increasing the fractions of Fe and Mn typically results in larger, less agglomerated particles, as observed in MFN-D and E. In contrast, Ni-rich systems tend to produce smaller particles, as Ni enhances nucleation rates due to faster diffusion. Consequently, MFN-C, with a higher Ni/Mn ratio, includes particles as small as 500 – 600 nm.

The mixed particle morphology in MFN-C, characterized by both large and small particles, would present significant challenges. During slurry preparation, the size disparity between particles leads to non-uniform dispersion, with smaller particles dispersing homogeneously while larger particles tend to settle. This heterogeneity becomes more pronounced during the coating process, resulting in a non-uniform distribution of active material in the cathode, which detrimentally affects electrochemical performance. Therefore, balancing the Ni/Mn ratio is critical for controlling the morphology of layered oxides, which directly impacts their electrochemical performance. The EDS mapping in Figs. 4, S8, and S9 confirms that all elements are homogeneously distributed throughout the sample, confirming that the observed variations in morphology and particle size are intrinsic to the material composition rather than due to elemental segregation.

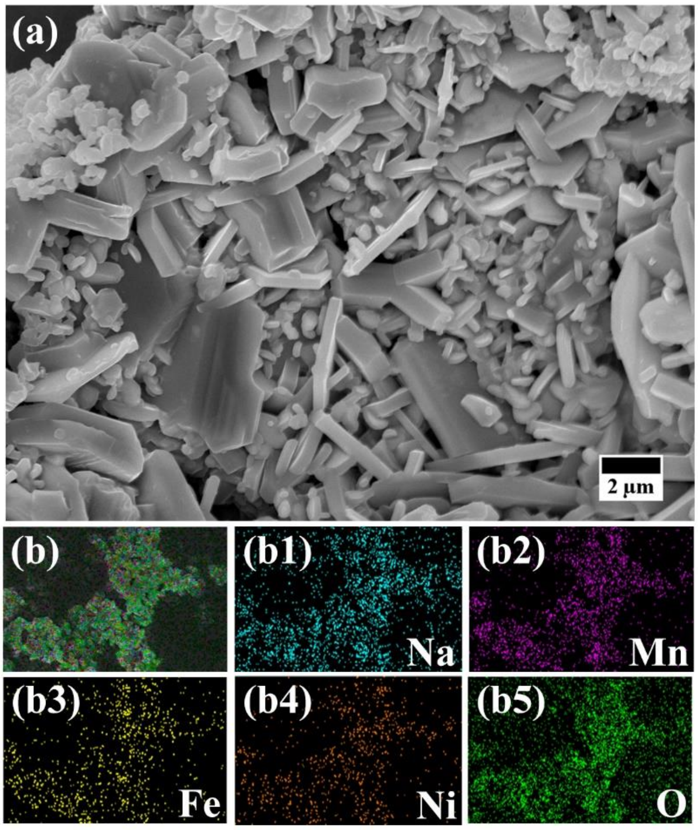

Fig. 4. (a) SEM micrograph of MFN-C sample calcined at 800°C. (b) EDS mapping indicating uniform distribution of constituent elements.

3.1.3. X-ray photoelectron spectroscopy

The oxidation states of Mn, Fe, and Ni in MFN-C, MFN-D, and MFN-E were verified using XPS, as shown in Fig. 5. The Mn 2p spectrum for MFN-C exhibits two distinct peaks at ~642.6 eV and ~653.7 eV, corresponding to Mn $2p_{3/2}$ and Mn $2p_{1/2}$, respectively. These binding energy values confirm the presence of Mn in the tetravalent state (Mn^{4+}) in MFN-C. As the Ni/Mn ratio decreases, the Mn spectra can be deconvoluted into four peaks: two associated with Mn^{3+} (Mn $2p_{3/2}$ at ~641.2 eV and Mn $2p_{1/2}$ at ~651.9 eV) and two corresponding to Mn^{4+} (Mn $2p_{3/2}$ at ~642.6 eV and Mn $2p_{1/2}$ at ~653.7 eV) [43, 55, 56]. Also, the Mn^{3+}/Mn^{4+} ratio increases from MFN-D to MFN-E. The Fe 2p spectrum displays two characteristic peaks at 710.7 eV and 724.2 eV, indicating the presence of Fe^{3+} ions in all samples [43, 55, 56]. Similarly, the Ni spectrum reveals peaks at 854.4 eV (Ni $2p_{3/2}$) and 872.1 eV (Ni $2p_{1/2}$), along with their associated shake-up satellites, confirming the presence of Ni in the divalent state (Ni^{2+}) in all samples [43, 55, 56].

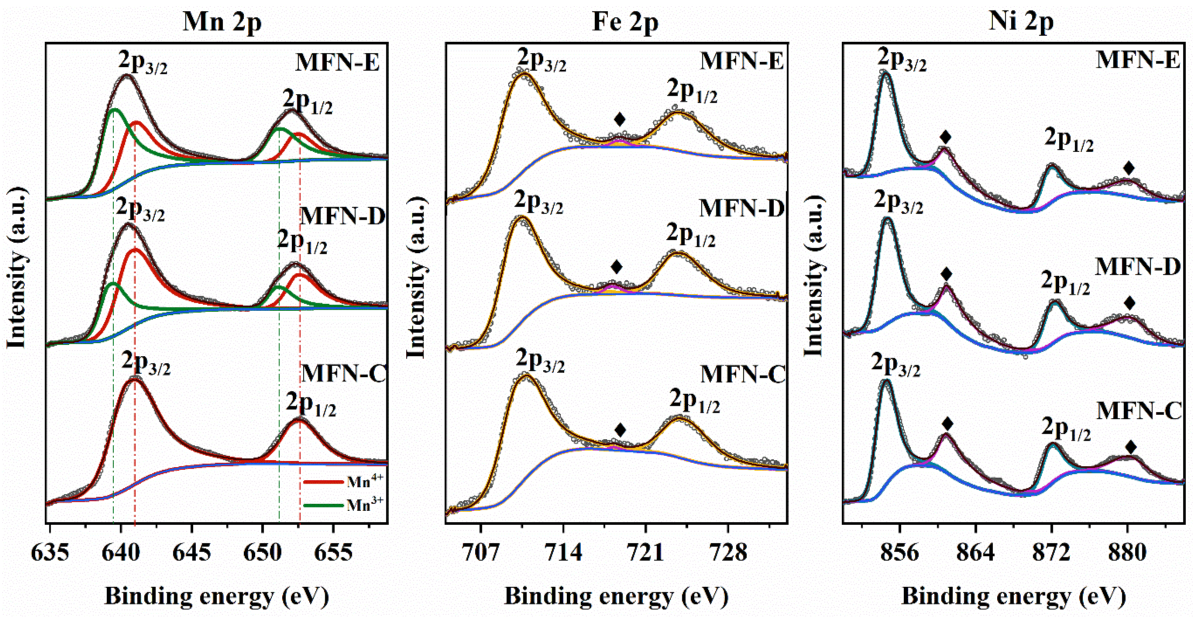

Fig. 5. Mn 2p spectra, Ni 2p spectra, and Fe 2p spectra of the MFN-C, D, and E samples. ♦ represents the shake-up satellite peaks in the Fe 2p and Ni 2p spectra.

3.2. Electrochemical characterization

3.2.1. Galvanostatic charge-discharge

The effects of phases and structural parameters on electrochemical performance were evaluated by testing all MFN samples in the 2.5 – 4.4 V range. The electrochemical properties for all calcination temperatures are summarized in Tables S34-S37. The voltage window (2.5 – 4.4 V) is chosen to investigate the effects of high voltage redox processes, namely the Ni^{2+}/Ni^{4+} and the Fe^{3+}/Fe^{4+} reactions, on the electrochemical properties. The GCD profiles at 0.1C are illustrated in Figs. 6(a) and S10-S12(a), with the corresponding dQ/dV vs. V curves represented in the pseudo-ternary diagrams in Figs. 6(b) and S10-S12(b).

Some important trends can be seen in the GCD curves for all calcination temperatures, such as the GCD profiles becoming more sloping, with the plateaus above 3.2 V merging together with increasing Fe content. This indicates that an increase in Fe content results in a solid solution reaction and the absence of Na^+/vacancy ordering upon sodiation/desodiation [43, 57]. Such behavior underscores the role of Fe in promoting homogeneous electrochemical reactions, minimizing phase transitions, and enhancing structural reversibility during cycling. Further, the specific capacity at 0.1C decreases as the Ni content decreases. The highest discharge capacity of 139.1 mAh g^{-1} was delivered by the $Na_{0.8}Mn_{0.53}Fe_{0.14}Ni_{0.33}O_2$ material when calcined at 800 °C, while the lowest capacity at this calcination temperature is found for $Na_{0.8}Mn_{0.75}Fe_{0.14}Ni_{0.11}O_2$ (89.7 mAh g^{-1}).

The dQ/dV curves undergo significant changes with variations in composition. The main redox peaks observed are peaks near 3.2 – 3.8 V (common for Ni^{2+}/Ni^{4+}) [34, 35], and peaks above 4.1 – 4.2 V (may be attributed to Fe^{3+}/Fe^{4+}) [33]. These peak attributions are well-established in the literature [7, 45-48]. Figs. 6(b) and S10-S12(b) demonstrate that the redox activity in $Na_{0.8}$(Mn-Fe-Ni)O_2 cathodes is highly dependent on the composition. For instance, the Ni^{2+}/Ni^{4+} redox peaks grow with increasing Ni contents. The dQ/dV curves for MFN-G and MFN-F, with the least amount of Fe, show multiple peaks corresponding to Na-ion/vacancy ordering rearrangements that occur during cycling in accordance with the GCD results. Also, for compositions on the constant Fe lines, a decreasing Ni/Mn ratio makes the dQ/dV curves smoother, which corresponds to fewer phase transitions during electrochemical cycling and thereby leads to better cyclability. Interestingly, for certain compositions, such as MFN-A and MFN-D, the dQ/dV curves for samples calcined at lower calcination temperature (700 °C) have several peaks that become smooth as the calcination temperature increases to 1000 °C. At ~4.3 V, high-voltage peaks are found for all compositions, which are commonly found for layered oxides. Several processes can contribute to this peak, e.g., phase transformations [58, 59], formation of new phases [3, 37, 39, 60], or contributions from anionic redox of lattice oxygen ($O^{2-} \rightarrow O_2^-$) [61, 62].

The average voltage is a key parameter influencing the overall energy density of the cathode material. For layered oxide cathodes, the average discharge voltage generally ranges from 2.3 to 3.5 V [63]. Cathodes containing high-voltage redox-active transition metals, such as Ni and Fe, tend to exhibit higher average voltages. The average voltage values of the MFN samples calcined at various calcination temperatures are given in Tables S34-S37. Among the samples calcined at 800 °C, MFN-D, MFN-G, and MFN-A exhibit average discharge voltages of 3.6 V, 3.54 V, and 3.48 V, respectively. The high specific capacities of MFN-A (134.2 mAh g^{-1}) and MFN-D (127.3 mAh g^{-1}), combined with their elevated average discharge voltages, contribute to high specific energies. As a result, the energy densities of these cathodes approach 460 Wh kg^{-1} at the cathode active material level.

3.2.2. Rate performance

Figs. 6(c) and S10-S12(c) display the rate capabilities of MFN samples at various C-rates in the 0.1C to 5C range. The percentage capacity retention at 0.2C and 1C compared to 0.1C is summarized in Tables S34-S37. Significant variations in rate performance are attributed to the distinct local environments created by varying transition metal ratios and the effects of calcination temperature, which influence the degree of particle agglomeration and average particle size in these samples. The materials synthesized at 700 °C and 800 °C exhibited superior rate capabilities, demonstrated by higher capacity retention at both 0.2C and 1C. The superior rate capability is attributed to reduced particle agglomeration and smaller particle sizes, facilitating more efficient ion transport. Most samples retained above 80% of their initial capacity at 0.2C, while capacity retention at 1C ranged from 51% to 74%.

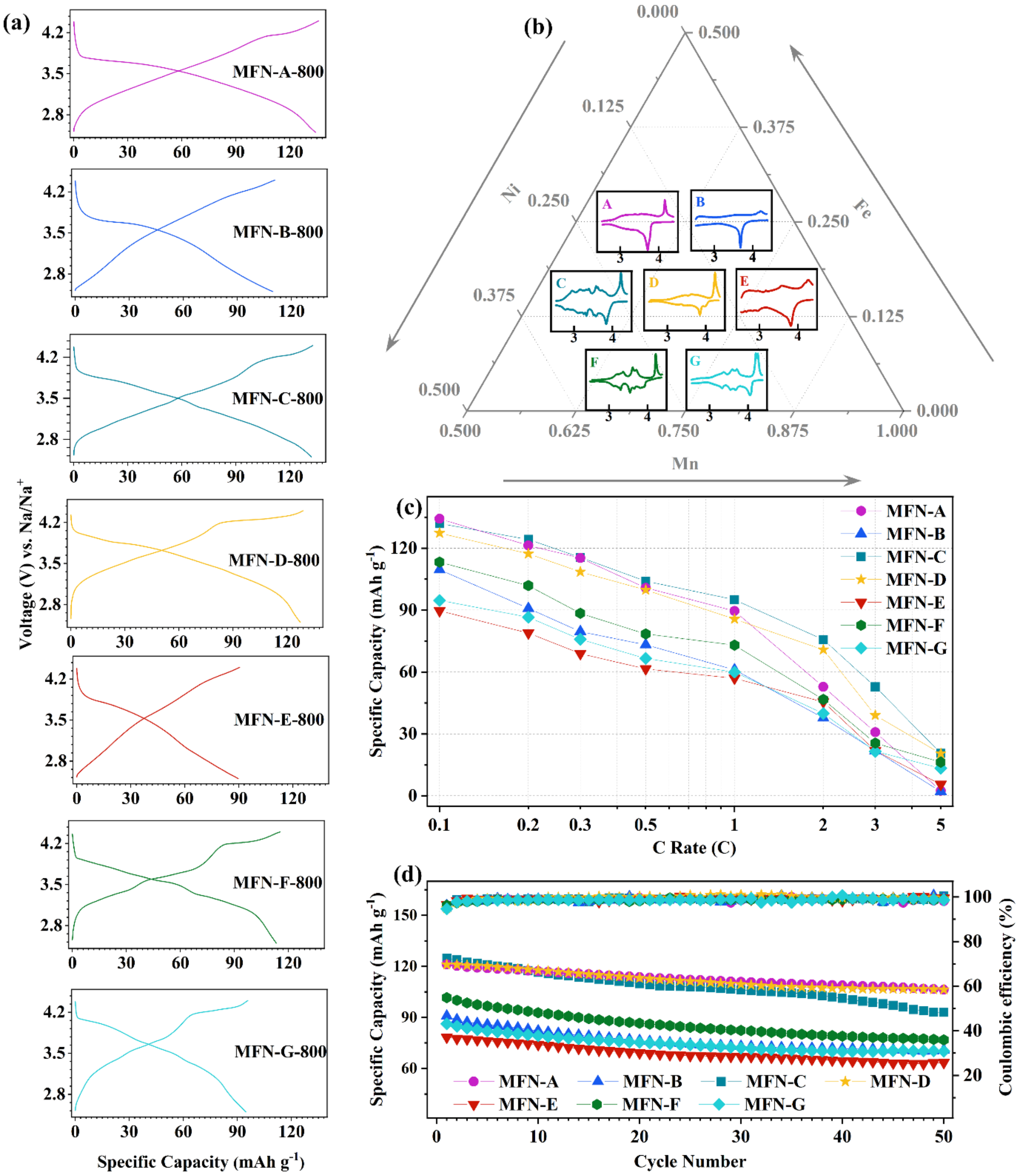

Fig. 6. (a) Galvanostatic charge-discharge curves at 0.1C, (b) dQ/dV vs. V profiles, (c) rate performance, and (d) cyclic stability of MFN samples calcined at 800 °C.

At higher synthesis temperatures of 900 °C and 1000 °C, a noticeable decline in rate performance was observed compared to lower temperatures. At 900 °C, retention at 0.2C dropped to 77 – 84%, while at 1C, capacity retention fell significantly to 36 – 52%. The capacity depletion at higher C-rates became more pronounced at 1000 °C, with capacity retention at 1C plummeting to 10% for MFN-B. Despite the decline, MFN-D outperformed other samples at 1C, though its rate capability remained significantly lower than those synthesized at 700 °C or 800 °C. The overall trend reveals that higher calcination temperatures (900 °C and 1000 °C) significantly increase particle agglomeration, severely limiting Na^+ diffusion and degrading rate performance. This underscores the critical role of particle size and agglomeration in determining the electrochemical behavior of these materials.

3.2.3. Cyclability

The cyclability of MFN samples at 0.2C is presented in Figs. 6(d) & S10-12(d) and summarized in Tables S34-S37. Additionally, the cycling performance of MFN-C, D, and E samples calcined at 800 °C was further evaluated at 1C, and the results are shown in Fig. S13. Higher capacity retention in samples synthesized at lower calcination temperatures can be attributed to reduced agglomeration and optimal particle sizes, which preserve the structural integrity. Among the samples, MFN-D exhibited superior cyclability across all synthesis temperatures, retaining over 88% of its initial capacity after 50 cycles at 700 °C and 800 °C. This performance underscores its exceptional structural stability. An increased Ni/Mn ratio along constant Fe-content lines resulted in higher specific capacities but compromised cyclic stability, particularly for samples calcined at higher temperatures. For example, MFN-C exhibited excellent cyclic performance at lower synthesis temperatures but experienced significant degradation at 900 °C and 1000 °C. Conversely, with a low Ni/Mn ratio, MFN-E exhibited decent cycling stability at 900 °C. At 1C, the capacity retention for MFN-C, D, and E calcined at 800 °C was 76%, 89%, and 81%, respectively, further confirming the excellent superior high-rate cycling stability of MFN-D. Overall, a higher Ni/Mn ratio enhances the specific capacity, a lower ratio improves structural stability (consequently, cyclic performance), and diminishes the rate performance, particularly for the P2 phases formed at higher calcination temperatures. This trade-off makes materials with a low Ni/Mn ratio better suited for applications requiring long-term stability and lower rates of discharge, such as in grid storage or backup power systems. MFN-D, with its balance of high capacity and stability, is more suited for high-power applications like electric vehicles and portable electronics, where both performance and durability are crucial.

3.2.4. Galvanostatic intermittent titration technique

The sodium-ion diffusion coefficient (D_{Na+}) was evaluated using the galvanostatic intermittent titration technique (GITT). The GITT curves and corresponding diffusion coefficient values for MFN-C, MFN-D, and MFN-E are shown in Fig. 7. Prior to the GITT measurements, the cells underwent the initial formation cycle. For the GITT measurements, cells were subjected to a constant current pulse at 0.1C for 10 minutes, followed by a 30-minute relaxation period to allow the cathodes to reach a pseudo-equilibrium state. The diffusion process is assumed to adhere to Fick's first law of diffusion. The D_{Na+} values are calculated using the following equation (1) [64]:

$$D_{Na^+} = \frac{4}{\pi\tau}\left(\frac{m_B V_m}{M_B S}\right)^2 \left(\frac{\Delta E_S}{\Delta E_\tau}\right)^2 \qquad (t \ll L^2 / D) \qquad \ldots\ldots\ldots\ldots\ldots(1)$$

where:

- τ is the duration of the constant current pulse,
- m_B is the active material loading on the cathode,
- V_m is the molar volume of the material,
- M_B is the molecular weight of the material,
- S is the surface area of the cathode,
- ΔE_τ is the voltage change during the current pulse,
- ΔE_S is the voltage change when the material reaches equilibrium.

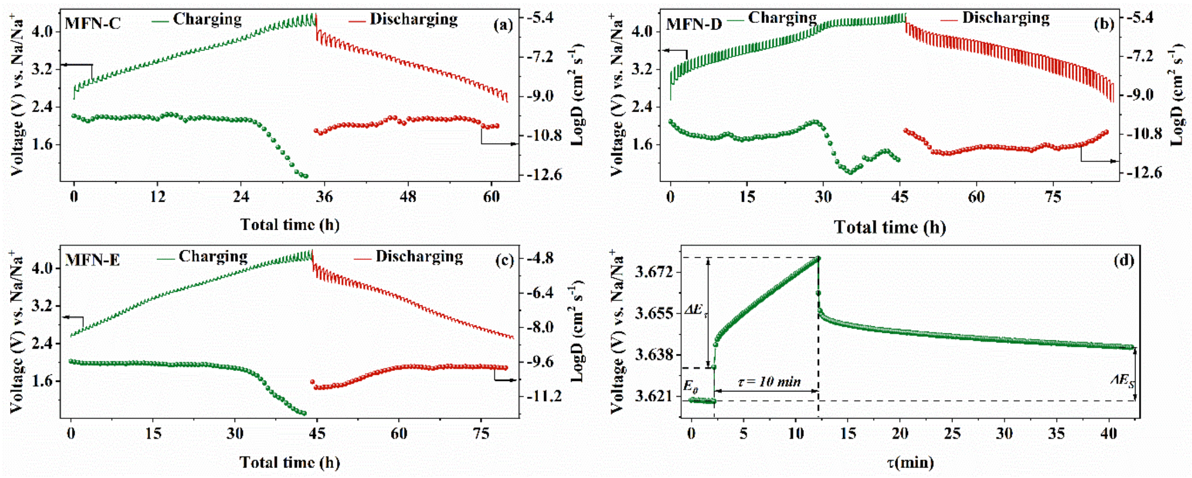

Fig. 7. GITT profiles of (a) MFN-C, (b) MFN-D, and (c) MFN-E at 0.1C, along with the variations in diffusion coefficients during charge-discharge. (d) A single titration unit of the GITT curve showing the variables considered in Equation 1.

Analysis revealed that the diffusion coefficients are higher in the better-performing MFN-D sample. Fig. 7 shows that the Na-ion diffusion coefficient has lower values at higher voltages when the cathode contains fewer Na-ions, indicating slower kinetics at these voltages. This highlights the advantage of the optimal Ni/Mn ratio in enhancing electrochemical performance.

3.2.5. *Operando* Synchrotron XRD

The structural stability of the samples was confirmed using *operando* Synchrotron XRD measurements during cycling. Synchrotron XRD patterns were recorded for MFN-D and MFN-E cathodes at a charge/discharge rate of 0.2C in the 2.5 – 4.4 V voltage range, as shown in Figs. 8(a) and S14(a). The corresponding galvanostatic charge-discharge (GCD) profiles are shown in Figs. 8(b) and S14(b), while contour maps highlighting selected 2θ regions extracted from the operando XRD data are presented in Figs. 8(c-e) and S14(c-e). During charging, the (002) and (004) diffraction peaks of the P2 phase shift towards lower angles, attributed to the lattice expansion along the *c*-direction due to increased electrostatic repulsion between the layers. The P2 (100) peak at $2\theta \approx 16.6°$ and the P2 (102) peak at $2\theta \approx 18.3°$ shift to higher angles, indicating a contraction of the *a*-lattice parameter in the P2 phase for both samples. Upon discharge, all diffraction peaks return to their initial positions, with no new peaks observed during the charge/discharge process.

P-type layered compounds are well known to undergo a P-to-O phase transition at high states of charge, which induces severe irreversible structural degradation over long-term cycling [65-67]. In conventional P2-type cathode materials, this transition typically occurs above 4.2 V, forming a metastable O2 phase that facilitates the gliding of transition metal TM slabs and subsequent structural distortion. Studies have demonstrated that strategic cation substitution can alter this transformation pathway, enabling a P2-to-OP4 transition instead. The OP4 phase exhibits reduced lattice contraction, offering improved structural reversibility. Despite its reversibility, repeated P2-to-OP4 transitions introduce cumulative strain, potentially accelerating structural failure, as any formation of an O-type layer in a P2-phase cathode inherently induces lattice contraction. In MFN-D and MFN-E, the optimized TM ratios effectively suppress high-voltage phase transitions of the P2 phase. However, subtle structural changes are observed beyond 4.2 V, where the (004), (100), and (102) diffraction peaks broaden and weaken until the end of charge (highlighted by thick lines in the operando XRD patterns, Figs. 8(a) and S14(a)). This suggests a degree of structural modification without the emergence of a distinct new phase [68, 69]. Notably, in MFN-E, the P2 diffraction peak broadening and weakening occur at a significantly lower voltage (~3.1 V) than in MFN-D, indicating an earlier onset of structural alteration in MFN-E.

The lattice parameter variations during charge/discharge were quantified using LeBail refinement of the *operando* Synchrotron XRD data at different voltages. The trends in the *a* and *c* parameters are illustrated in Figs. 8(f, g) and S14(f, g). The evolution of the *c* parameter follows the well-established behavior of layered oxides, characterized by expansion and contraction along the *c* axis during charging and discharging, respectively [36, 70]. The change in the *c* parameter ($\Delta c = \frac{c_{4.4V} - c_{2.5V}}{c_{4.4V}} \times 100\%$) of the P2 phase is ~ -1.6% in MFN-D and ~ -2.0% in MFN-E during discharging from 4.4 V to 2.5 V. A well-balanced ratio of transition metals combined with structural benefits in MFN-D supports superior structural integrity, contributing to excellent capacity retention in this material.

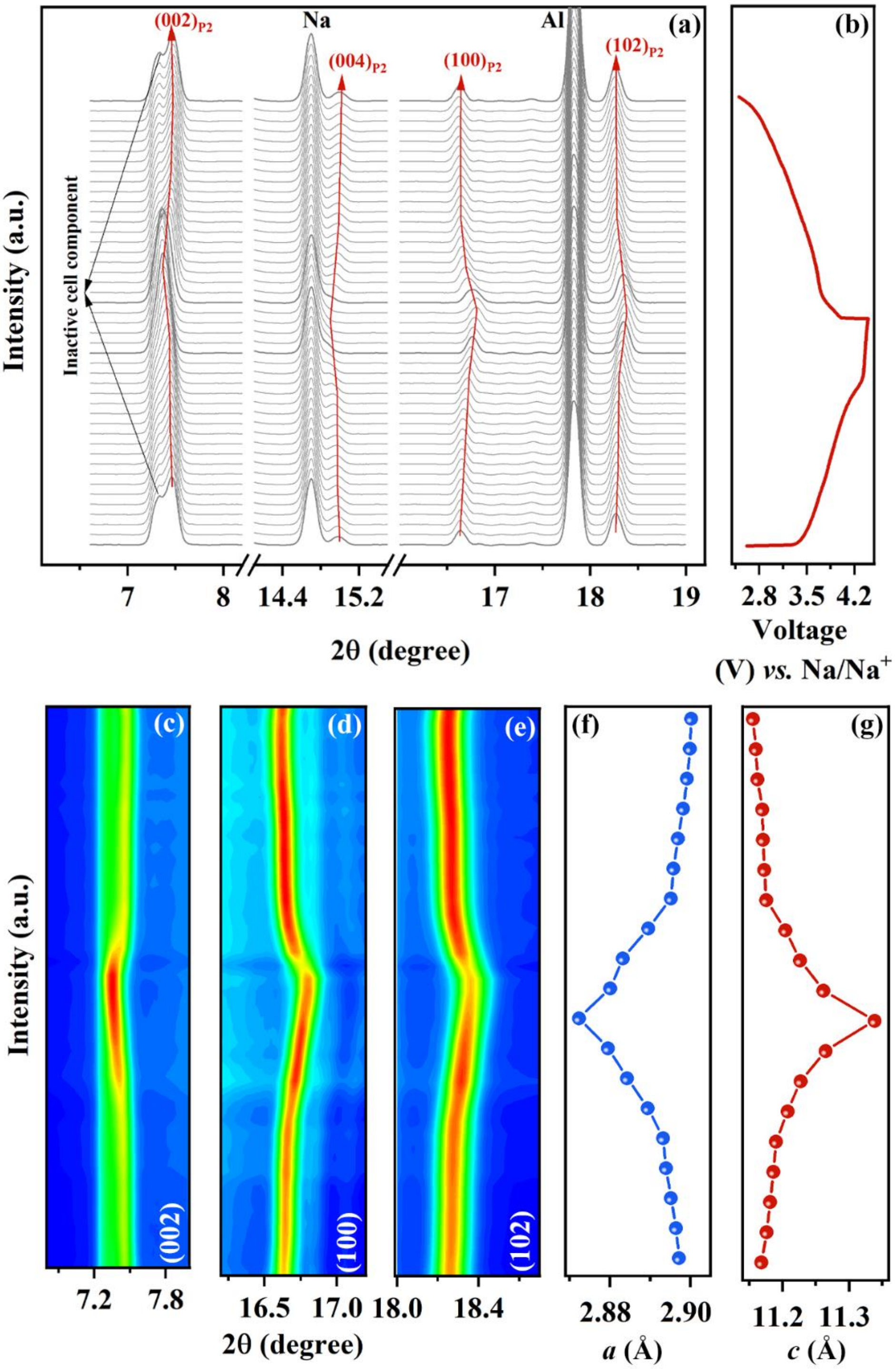

Fig. 8. (a) *Operando* synchrotron XRD patterns of MFN-D. (b) The corresponding GCD curve showing various states of charge/discharge. Color contour maps highlighting (c) (002), (d) (100), and (e) (102) peaks of the P2 phase of MFN-D. Variation in (f) *a* parameter and (g) *c* parameter of the P2 phase during charge/discharge.

The structural stability of the MFN-D and MFN-E samples was further evaluated by subjecting them to ambient air exposure for 30 days. Comparative analysis of the XRD patterns before and after exposure showed no observable changes (Figs. S15 and S16). This demonstrates the exceptional moisture stability of these materials, enabling their storage under ambient conditions, thereby reducing the fabrication cost of cells.

3.3. Key design insights for high voltage Na-ion cathodes

The findings of this study offer valuable insights into the design of high-voltage Na-ion cathodes, emphasizing the critical influence of transition metal composition and particle morphology on structural and electrochemical performance. Precise control over the Ni/Mn ratio modulates the balance between redox activity and structural robustness, thereby acting as an essential design parameter for simultaneously optimizing specific capacity, rate capability, and cycling stability. Higher Ni content promotes higher specific capacities through enhanced redox activity at elevated voltages, while Mn contributes to structural stability. The calcination temperature also plays a pivotal role, with lower temperatures (700 – 800 °C) yielding superior rate capability and cycling stability due to reduced particle agglomeration and optimal particle sizes. Furthermore, the dominance of the P2 phase facilitates rapid Na-ion diffusion through prismatic sites, enhancing electrochemical kinetics. Electrochemical characterization revealed that reducing the Ni/Mn ratio along constant Fe lines improves structural stability and cycling performance at the cost of specific capacity and high-rate performance. To provide a consolidated overview of these trends, a comparative bar graph is presented in Fig. S17, which visually summarizes the variation in specific capacity, rate performance, and cycling stability across MFN compositions at different calcination temperatures. Overall, P2-type $Na_{0.8}Mn_{0.64}Fe_{0.14}Ni_{0.22}O_2$, calcined at 800 °C, is identified as the optimal composition that exhibits excellent electrochemical performance as a cathode material for sodium-ion batteries.

4. CONCLUSIONS

This study systematically explores the effects of calcination temperature and transition metal composition on the structural, morphological, and electrochemical properties of $Na_{0.8}$(Mn-Fe-Ni)O_2 layered oxides, aiming to establish an optimized framework for cathode design for sodium-ion batteries.

- XRD data revealed that the calcination temperature plays a critical role in determining the phase composition of the material. At lower temperatures (700 °C), the P3 phase dominates, particularly in Fe- and Mn-rich compositions. However, as the calcination temperature increases to 800 °C and beyond, a clear preference toward the P2 phase is observed. The Fe-rich compositions favor the O3 phase, while Mn-rich samples promote the coexistence of P2 and P3 phases due to repulsion between oxygen ions and promoting the formation of prismatic sites.

- The lattice parameters reveal that increasing Ni content causes a decrease in the *c* parameter, while higher Mn and Fe expand it.
- The FESEM analysis reveals that Ni-rich samples exhibit particles ranging from 500 nm to 2.4 µm, whereas Fe/Mn-rich samples show larger, less agglomerated particles.

The electrochemical studies unveiled the following trends:

- Materials with higher Ni content showed higher specific discharge and average voltages, leading to elevated specific energies (~460 Wh kg^{-1} at the cathode active material level).
- The highest discharge capacity of ~139 mAh g^{-1} was achieved by the $Na_{0.8}Mn_{0.53}Fe_{0.14}Ni_{0.33}O_2$ sample calcined at 800 °C, followed by $Na_{0.8}Mn_{0.64}Fe_{0.14}Ni_{0.22}O_2$ (124.5 mAh g^{-1} at 0.1C), while the lowest capacity (89.7 mAh g^{-1}) was observed for the $Na_{0.8}Mn_{0.75}Fe_{0.14}Ni_{0.11}O_2$ sample.
- As the Fe content increases, the GCD profiles become more sloping, indicating that higher Fe content fosters a solid solution reaction mechanism, suppressing the Na^{+}/vacancy ordering usually observed during sodiation/desodiation. For compositions along constant Fe-content lines, a decrease in the Ni/Mn ratio results in smoother GCD and dQ/dV curves, resulting in enhanced cyclability.
- Samples calcined at 700 °C and 800 °C exhibited much better rate capabilities, retaining over 80% of their capacity at 0.2C and 51% – 74% at 1C.
- In contrast, samples calcined at 900 °C and 1000 °C showed a significant decline in capacity retention, with some compositions retaining as low as 10% of their initial capacity.
- $Na_{0.8}Mn_{0.64}Fe_{0.14}Ni_{0.22}O_2$ demonstrated the best performance across all calcination temperatures, with high capacity retention and excellent cyclability, retaining more than 88% of its initial capacity after 50 cycles.

The synchrotron XRD analysis revealed the absence of phase transitions in the MFN-D and MFN-E samples calcined at 800 °C during cycling, which contributes to enhanced structural stability. Quantification of the change in the *c* parameter reveals that $Na_{0.8}Mn_{0.64}Fe_{0.14}Ni_{0.22}O_2$ experiences less strain during charge/discharge, which directly correlates with its higher capacity retention and better electrochemical performance. These findings underscore the pivotal role of optimizing transition metal ratios and calcination temperature to achieve desired structural and electrochemical properties, paving the way for improved energy storage solutions.

CRediT authorship contribution statement

Samriddhi Saxena: Conceptualization, Data curation, Formal analysis, Investigation, Methodology, Validation, Writing – original draft. **Hari Narayanan Vasavan:** Data curation, Writing – review & editing. **Neha Dagar:** Writing – review & editing. **Velaga Srihari:** Writing – review & editing. **Asish Kumar Das:** Writing – review & editing. **Pratiksha Gami:** Writing – review & editing. **Sonia Deswal:** Writing – review & editing. **Pradeep Kumar:** Writing – review & editing. **Himanshu Kumar Poswal:** Writing – review & editing. **Sunil Kumar:** Funding acquisition, Project administration, Supervision, Validation, Writing – review & editing.

Declaration of competing interest

The authors declare that they have no known competing financial interests or personal relationships that could have appeared to influence the work reported in this paper.

Acknowledgments

This work was financially supported by the Ministry of Education, Government of India (grant number: MoE-STARS/STARS-2/2023-0365). SS thanks the Ministry of Education, Government of India, for the Prime Minister’s Research Fellowship (grant number: 2103359).

Data availability

Data will be made available on request.

REFERENCES

1. Mohammed Ibrahim Jamesh, A. S. Prakash, *"Advancement of technology towards developing Na-ion batteries"*, **Journal of Power Sources** 378 (2018) 268-300. https://doi.org/10.1016/j.jpowsour.2017.12.053.
2. Jianqiu Deng, Wen-Bin Luo, Shu-Lei Chou, Hua-Kun Liu, Shi-Xue Dou, *"Sodium-Ion Batteries: From Academic Research to Practical Commercialization"*, **Advanced Energy Materials** 8(4) (2018) 1701428. https://doi.org/10.1002/aenm.201701428.
3. Eider Goikolea, Verónica Palomares, Shijian Wang, Idoia Ruiz de Larramendi, Xin Guo, Guoxiu Wang, Teofilo Rojo, *"Na-Ion Batteries—Approaching Old and New Challenges"*, **Advanced Energy Materials** 10(44) (2020) 2002055. https://doi.org/10.1002/aenm.202002055.
4. Ting Jin, Huangxu Li, Kunjie Zhu, Peng-Fei Wang, Pei Liu, Lifang Jiao, *"Polyanion-type cathode materials for sodium-ion batteries"*, **Chemical Society Reviews** 49(8) (2020) 2342-2377. https://doi.org/10.1039/C9CS00846B.
5. Sung-Wook Kim, Dong-Hwa Seo, Xiaohua Ma, Gerbrand Ceder, Kisuk Kang, *"Electrode Materials for Rechargeable Sodium-Ion Batteries: Potential Alternatives to Current Lithium-Ion Batteries"*, **Advanced Energy Materials** 2(7) (2012) 710-721. https://doi.org/10.1002/aenm.201200026.
6. Zhigao Chen, Yuyu Deng, Ji Kong, Weibin Fu, Chenyang Liu, Ting Jin, Lifang Jiao, *"Toward the High-Voltage Stability of Layered Oxide Cathodes for Sodium-Ion Batteries: Challenges, Progress, and Perspectives"*, **Advanced Materials** 36(26) (2024) 2402008. https://doi.org/10.1002/adma.202402008.
7. Ivana Hasa, Daniel Buchholz, Stefano Passerini, Jusef Hassoun, *"A Comparative Study of Layered Transition Metal Oxide Cathodes for Application in Sodium-Ion Battery"*, **ACS Applied Materials & Interfaces** 7(9) (2015) 5206-5212. https://doi.org/10.1021/am5080437.
8. C. Delmas, C. Fouassier, P. Hagenmuller, *"Structural classification and properties of the layered oxides"*, **Physica B+C** 99(1) (1980) 81-85. https://doi.org/10.1016/0378-4363(80)90214-4.
9. Kei Kubota, Shinichi Kumakura, Yusuke Yoda, Kazutoshi Kuroki, Shinichi Komaba, *"Electrochemistry and Solid-State Chemistry of $NaMeO_2$ (Me = 3d Transition Metals)"*, **Advanced Energy Materials** 8(17) (2018) 1703415. https://doi.org/10.1002/aenm.201703415.
10. Xiaobo Zheng, Peng Li, Haojie Zhu, Kun Rui, Guoqiang Zhao, Jie Shu, Xun Xu, Wenping Sun, Shi Xue Dou, *"New insights into understanding the exceptional electrochemical performance of P2-type manganese-based layered oxide cathode for sodium ion batteries"*, **Energy Storage Materials** 15 (2018) 257-265. https://doi.org/10.1016/j.ensm.2018.05.001.
11. Shaohua Guo, Yang Sun, Jin Yi, Kai Zhu, Pan Liu, Yanbei Zhu, Guo-zhen Zhu, Mingwei Chen, Masayoshi Ishida, Haoshen Zhou, *"Understanding sodium-ion diffusion in layered P2 and P3 oxides via experiments and first-principles calculations: a bridge between crystal structure and electrochemical performance"*, **NPG Asia Materials** 8(4) (2016) e266-e266. https://doi.org/10.1038/am.2016.53.
12. Raphaële J. Clément, Peter G. Bruce, Clare P. Grey, *"Review—Manganese-Based P2-Type Transition Metal Oxides as Sodium-Ion Battery Cathode Materials"*, **Journal of the Electrochemical Society** 162(14) (2015) A2589. https://doi.org/10.1149/2.0201514jes.
13. Shipeng Jia, Jonathan Counsell, Michel Adamič, Antranik Jonderian, Eric McCalla, *"High-throughput design of Na–Fe–Mn–O cathodes for Na-ion batteries"*, **Journal of Materials Chemistry A** 10(1) (2022) 251-265. https://doi.org/10.1039/D1TA07940A.
14. Zhengbo Liu, Jun Liu, *"Structural Evolution in P2-type Layered Oxide Cathode Materials for Sodium-Ion Batteries"*, **ChemNanoMat** 8(2) (2022) e202100385. https://doi.org/10.1002/cnma.202100385.
15. Xiaowei Ma, Chen Yang, Ziyang Xu, Ruiqi Li, Li Song, Mingdao Zhang, Mei Yang, Yachao Jin, *"Structural and electrochemical progress of O3-type layered oxide cathodes for*

Na-ion batteries", **Nanoscale** 15(36) (2023) 14737-14753. https://doi.org/10.1039/D3NR02373G.
16. Xinghan Li, Yameng Fan, Bernt Johannessen, Xun Xu, Khay Wai See, Wei Kong Pang, *"O3-Type Cathodes for Sodium-Ion Batteries: Recent Advancements and Future Perspectives"*, **Batteries & Supercaps** 7(5) (2024) e202300618. https://doi.org/10.1002/batt.202300618.
17. Dingbang Hao, Gaoyuan Zhang, De Ning, Dong Zhou, Yan Chai, Jin Xu, Xingxing Yin, Ruijie Du, Götz Schuck, Jun Wang, Yongli Li, *"Design of high-entropy P2/O3 hybrid layered oxide cathode material for high-capacity and high-rate sodium-ion batteries"*, **Nano Energy** 125 (2024) 109562. https://doi.org/10.1016/j.nanoen.2024.109562.
18. Ziqing Wang, Lei Fang, Xiaoguang Fu, Shengfeng Zhang, Huabin Kong, Hongwei Chen, Fang Fu, *"A Ni/Co-free high-entropy layered cathode with suppressed phase transition and near-zero strain for high-voltage sodium-ion batteries"*, **Chemical Engineering Journal** 480 (2024) 148130. https://doi.org/10.1016/j.cej.2023.148130.
19. Hari Narayanan Vasavan, Manish Badole, Samriddhi Saxena, Velaga Srihari, Asish Kumar Das, Pratiksha Gami, Neha Dagar, Sonia Deswal, Pradeep Kumar, Himanshu Kumar Poswal, Sunil Kumar, *"Identification of optimal composition with superior electrochemical properties along the zero* Mn^{3+} *line in* $Na_{0.75}(Mn\text{-}Al\text{-}Ni)O_2$ *pseudo ternary system"*, **Journal of Energy Chemistry** 96 (2024) 206-216. https://doi.org/10.1016/j.jechem.2024.04.015.
20. Samriddhi Saxena, Manish Badole, Hari Narayanan Vasavan, Velaga Srihari, Asish Kumar Das, Pratiksha Gami, Sonia Deswal, Pradeep Kumar, Sunil Kumar, *"Deciphering the role of optimal P2/O3 phase fraction in enhanced cyclability and specific capacity of layered oxide cathodes"*, **Chemical Engineering Journal** 485 (2024) 149921. https://doi.org/10.1016/j.cej.2024.149921.
21. Marlou Keller, Tobias Eisenmann, Debora Meira, Giuliana Aquilanti, Daniel Buchholz, Dominic Bresser, Stefano Passerini, *"In Situ Investigation of Layered Oxides with Mixed Structures for Sodium-Ion Batteries"*, **Small Methods** 3(11) (2019) 1900239. https://doi.org/10.1002/smtd.201900239.
22. Yuhang Zhuang, Jing Zhao, Yang Zhao, Xiaohui Zhu, Hui Xia, *"Carbon-coated single crystal O3-*$NaFeO_2$ *nanoflakes prepared via topochemical reaction for sodium-ion batteries"*, **Sustainable Materials and Technologies** 28 (2021) e00258. https://doi.org/10.1016/j.susmat.2021.e00258.
23. Julia Lamb, Arumugam Manthiram, *"Surface-Modified* $Na(Ni_{0.3}Fe_{0.4}Mn_{0.3})O_2$ *Cathodes with Enhanced Cycle Life and Air Stability for Sodium-Ion Batteries"*, **ACS Applied Energy Materials** 4(10) (2021) 11735-11742. https://doi.org/10.1021/acsaem.1c02485.
24. Zelin Ma, Zeqin Zhao, Hanxue Xu, Jie Sun, Xuexia He, Zhibin Lei, Zong-huai Liu, Ruibin Jiang, Qi Li, *"A Queue-Ordered Layered Mn-Based Oxides with Al Substitution as High-Rate and High-Stabilized Cathode for Sodium-Ion Batteries"*, **Small** 17(6) (2021) 2006259. https://doi.org/10.1002/smll.202006259.
25. Xiaoyu Zhang, Yu Qiao, Shaohua Guo, Kezhu Jiang, Sheng Xu, Hang Xu, Peng Wang, Ping He, Haoshen Zhou, *"Manganese-Based Na-Rich Materials Boost Anionic Redox in High-Performance Layered Cathodes for Sodium-Ion Batteries"*, **Advanced Materials** 31(27) (2019) 1807770. https://doi.org/10.1002/adma.201807770.
26. Xiaohua Ma, Hailong Chen, Gerbrand Ceder, *"Electrochemical Properties of Monoclinic* $NaMnO_2$*"*, **Journal of the Electrochemical Society** 158(12) (2011) A1307. https://doi.org/10.1149/2.035112jes.
27. Naoaki Yabuuchi, Hiroaki Yoshida, Shinichi Komaba, *"Crystal Structures and Electrode Performance of Alpha-*$NaFeO_2$ *for Rechargeable Sodium Batteries"*, **Electrochemistry** 80(10) (2012) 716-719. https://doi.org/10.5796/electrochemistry.80.716.
28. Eungje Lee, Dennis E. Brown, Esen E. Alp, Yang Ren, Jun Lu, Jung-Je Woo, Christopher S. Johnson, *"New Insights into the Performance Degradation of Fe-Based Layered Oxides in*

Sodium-Ion Batteries: Instability of Fe^{3+}/Fe^{4+} Redox in α-$NaFeO_2$", **Chemistry of Materials** 27(19) (2015) 6755-6764. https://doi.org/10.1021/acs.chemmater.5b02918.

29. Junichiro Kugai, Hirotaka Mine, Satoshi Seino, Takashi Nakagawa, Takao A. Yamamoto, Hirohisa Yamada, *"Effects of sodium nitrate and heat treatment atmosphere on the synthesis of α–$NaFeO_2$ layered oxide"*, **Materials Chemistry and Physics** 249 (2020) 122948. https://doi.org/10.1016/j.matchemphys.2020.122948.

30. Kei Kubota, Takuya Asari, Hiroaki Yoshida, Naoaki Yaabuuchi, Hiromasa Shiiba, Masanobu Nakayama, Shinichi Komaba, *"Understanding the Structural Evolution and Redox Mechanism of a $NaFeO_2$–$NaCoO_2$ Solid Solution for Sodium-Ion Batteries"*, **Advanced Functional Materials** 26(33) (2016) 6047-6059. https://doi.org/10.1002/adfm.201601292.

31. Maider Zarrabeitia, Francesco Nobili, Oier Lakuntza, Javier Carrasco, Teófilo Rojo, Montse Casas-Cabanas, Miguel Ángel Muñoz-Márquez, *"Role of the voltage window on the capacity retention of P2-$Na_{2/3}[Fe_{1/2}Mn_{1/2}]O_2$ cathode material for rechargeable sodium-ion batteries"*, **Communications Chemistry** 5(1) (2022) 11. https://doi.org/10.1038/s42004-022-00628-0.

32. Ying Bai, Lixiang Zhao, Chuan Wu, Hui Li, Yu Li, Feng Wu, *"Enhanced Sodium Ion Storage Behavior of P2-Type $Na_{2/3}Fe_{1/2}Mn_{1/2}O_2$ Synthesized via a Chelating Agent Assisted Route"*, **ACS Applied Materials & Interfaces** 8(4) (2016) 2857-2865. https://doi.org/10.1021/acsami.5b11848.

33. Myungkyu Kim, Hyungjun Kim, Maenghyo Cho, Duho Kim, *"Theoretical understanding of oxygen stability in Mn–Fe binary layered oxides for sodium-ion batteries"*, **Journal of Materials Chemistry A** 10(20) (2022) 11101-11109. https://doi.org/10.1039/D2TA01747D.

34. Tim Risthaus, Dong Zhou, Xia Cao, Xin He, Bao Qiu, Jun Wang, Li Zhang, Zhaoping Liu, Elie Paillard, Gerhard Schumacher, Martin Winter, Jie Li, *"A high-capacity P2 $Na_{2/3}Ni_{1/3}Mn_{2/3}O_2$ cathode material for sodium ion batteries with oxygen activity"*, **Journal of Power Sources** 395 (2018) 16-24. https://doi.org/10.1016/j.jpowsour.2018.05.026.

35. Ryoichi Tatara, Hosei Suzuki, Mizuki Hamada, Kei Kubota, Shinichi Kumakura, Shinichi Komaba, *"Application of P2-$Na_{2/3}Ni_{1/3}Mn_{2/3}O_2$ Electrode to All-Solid-State 3 V Sodium(-Ion) Polymer Batteries"*, **The Journal of Physical Chemistry C** 126(48) (2022) 20226-20234. https://doi.org/10.1021/acs.jpcc.2c06360.

36. Jiaolong Zhang, Wenhui Wang, Wei Wang, Shuwei Wang, Baohua Li, *"Comprehensive Review of P2-Type $Na_{2/3}Ni_{1/3}Mn_{2/3}O_2$, a Potential Cathode for Practical Application of Na-Ion Batteries"*, **ACS Applied Materials & Interfaces** 11(25) (2019) 22051-22066. https://doi.org/10.1021/acsami.9b03937.

37. Elahe Talaie, Victor Duffort, Hillary L. Smith, Brent Fultz, Linda F. Nazar, *"Structure of the high voltage phase of layered P2-$Na_{2/3-z}[Mn_{1/2}Fe_{1/2}]O_2$ and the positive effect of Ni substitution on its stability"*, **Energy & Environmental Science** 8(8) (2015) 2512-2523. https://doi.org/10.1039/C5EE01365H.

38. Shinichi Komaba, Tetsuri Nakayama, Atsushi Ogata, Takaya Shimizu, Chikara Takei, S. Takada, A. Hokura, I. Nakai, *"Electrochemically Reversible Sodium Intercalation of Layered $NaNi_{0.5}Mn_{0.5}O_2$ and $NaCrO_2$"*, **ECS Transactions** 16(42) (2009) 43. https://doi.org/10.1149/1.3112727.

39. James W. Somerville, Adam Sobkowiak, Nuria Tapia-Ruiz, Juliette Billaud, Juan G. Lozano, Robert A. House, Leighanne C. Gallington, Tore Ericsson, Lennart Häggström, Matthew R. Roberts, Urmimala Maitra, Peter G. Bruce, *"Nature of the "Z"-phase in layered Na-ion battery cathodes"*, **Energy & Environmental Science** 12(7) (2019) 2223-2232. https://doi.org/10.1039/C8EE02991A.

40. Wenchao Qin, Yan Liu, Jinfeng Liu, Zihao Yang, Qiaoqiao Liu, *"Boosting the ionic transport and structural stability of Zn-doped O3-type $NaNi_{1/3}Mn_{1/3}Fe_{1/3}O_2$ cathode material for half/full sodium-ion batteries"*, **Electrochimica Acta** 418 (2022) 140357. https://doi.org/10.1016/j.electacta.2022.140357.

41. Donghan Kim, Eungje Lee, Michael Slater, Wenquan Lu, Shawn Rood, Christopher S. Johnson, *"Layered $Na[Ni_{1/3}Fe_{1/3}Mn_{1/3}]O_2$ cathodes for Na-ion battery application"*, **Electrochemistry Communications** 18 (2012) 66-69. https://doi.org/10.1016/j.elecom.2012.02.020.

42. Qiaoqiao Liu, Jinfeng Liu, Zihao Yang, Hongshun Miao, Yan Liu, *"A high rate and stability cathode material for half/full sodium-ion batteries: Nb-substituted $NaNi_{1/3}Mn_{1/3-x}Fe_{1/3}Nb_xO_2$ layered oxides"*, **Journal of Alloys and Compounds** 968 (2023) 172272. https://doi.org/10.1016/j.jallcom.2023.172272.

43. Sheng Feng, Chujun Zheng, Zhiyang Song, Xiangwei Wu, Meifen Wu, Fangfang Xu, Zhaoyin Wen, *"Boosting fast ionic transport and stability of O3-$NaNi_{1/3}Fe_{1/3}Mn_{1/3}O_2$ cathode via Al/Cu synergistically modulating microstructure for high-rate sodium-ion batteries"*, **Chemical Engineering Journal** 475 (2023) 146090. https://doi.org/10.1016/j.cej.2023.146090.

44. Shengxue Yan, Shaohua Luo, Liu Yang, Jian Feng, Pengwei Li, Qing Wang, Yahui Zhang, Xin Liu, *"Novel P2-type layered medium-entropy ceramics oxide as cathode material for sodium-ion batteries"*, **Journal of Advanced Ceramics** 11(1) (2022) 158-171. https://doi.org/10.1007/s40145-021-0524-8.

45. Marlou Keller, Daniel Buchholz, Stefano Passerini, *"Layered Na-Ion Cathodes with Outstanding Performance Resulting from the Synergetic Effect of Mixed P- and O-Type Phases"*, **Advanced Energy Materials** 6(3) (2016) 1501555. https://doi.org/10.1002/aenm.201501555.

46. Ji Ung Choi, Jae Hyeon Jo, Yun Ji Park, Kug-Seung Lee, Seung-Taek Myung, *"Mn-Rich P'2-$Na_{0.67}[Ni_{0.1}Fe_{0.1}Mn_{0.8}]O_2$ as High-Energy-Density and Long-Life Cathode Material for Sodium-Ion Batteries"*, **Advanced Energy Materials** 10(27) (2020) 2001346. https://doi.org/10.1002/aenm.202001346.

47. Hao Guo, Chenglong Zhao, Jianxiang Gao, Wenyun Yang, Xufeng Hu, Xiaobai Ma, Xuesheng Jiao, Jinbo Yang, Kai Sun, Dongfeng Chen, *"Slight Multielement Doping-Induced Structural Order–Disorder Transition for High-Performance Layered Na-Ion Oxide Cathodes"*, **ACS Applied Materials & Interfaces** 15(29) (2023) 34789-34796. https://doi.org/10.1021/acsami.3c04843.

48. Tianxiang Lan, Wenfei Wei, Shuai Xiao, Gang He, Jianhe Hong, *"P2-type Fe and Mn-based $Na_{0.67}Ni_{0.15}Fe_{0.35}Mn_{0.3}Ti_{0.2}O_2$ as cathode material with high energy density and structural stability for sodium-ion batteries"*, **Journal of Materials Science: Materials in Electronics** 31(12) (2020) 9423-9429. https://doi.org/10.1007/s10854-020-03482-9.

49. Aniruddh Ramesh, Abhinav Tripathi, Michel Bosman, Shibo Xi, Palani Balaya, *"Enhancement in rate performance and high voltage structural stability of P3/O3 $Na_{0.9}Fe_{0.5}Mn_{0.45}Ni_{0.05}O_2$ layered oxide cathode"*, **Journal of Electroanalytical Chemistry** 932 (2023) 117222. https://doi.org/10.1016/j.jelechem.2023.117222.

50. Samriddhi Saxena, Hari Narayanan Vasavan, Neha Dagar, Karthik Chinnathambi, Velaga Srihari, Asish Kumar Das, Pratiksha Gami, Sonia Deswal, Pradeep Kumar, Himanshu Kumar Poswal, Sunil Kumar, *"Probing the Compositional and Structural Effects on the Electrochemical Performance of Na(Mn-Fe-Ni)O_2 Cathodes in Sodium-Ion Batteries"*, **Battery Energy** e70018. https://doi.org/10.1002/bte2.20240083.

51. Alan A. Coelho, *"TOPAS and TOPAS-Academic: an optimization program integrating computer algebra and crystallographic objects written in C++"*, **Journal of Applied Crystallography** 51(1) (2018) 210-218. https://doi.org/10.1107/S1600576718000183.

52. Hari Narayanan Vasavan, Manish Badole, Samriddhi Saxena, Velaga Srihari, Asish Kumar Das, Pratiksha Gami, Sonia Deswal, Pradeep Kumar, Sunil Kumar, *"Impact of P3/P2 mixed phase on the structural and electrochemical performance of $Na_{0.75}Mn_{0.75}Al_{0.25}O_2$ cathode"*, **Journal of Energy Storage** 74 (2023) 109428. https://doi.org/10.1016/j.est.2023.109428.

53. Hari Narayanan Vasavan, Manish Badole, Samriddhi Saxena, Velaga Srihari, Asish Kumar Das, Pratiksha Gami, Sonia Deswal, Pradeep Kumar, Sunil Kumar, *"Unveiling the Potential of P3 Phase in Enhancing the Electrochemical Performance of a Layered Oxide Cathode"*, **Materials Today Energy** (2023) 101380. https://doi.org/10.1016/j.mtener.2023.101380.

54. Hari Narayanan Vasavan, Manish Badole, Samriddhi Saxena, Velaga Srihari, Asish Kumar Das, Pratiksha Gami, Neha Dagar, Sonia Deswal, Pradeep Kumar, Himanshu Kumar Poswal, Sunil Kumar, *"Rational design of an optimal Al-substituted layered oxide cathode for Na-ion batteries"*, **Electrochimica Acta** 494 (2024) 144457. https://doi.org/10.1016/j.electacta.2024.144457.

55. Jill Chastain, Roger C King Jr, *"Handbook of X-ray photoelectron spectroscopy"*, **Perkin-Elmer Corporation** 40 (1992) 221.

56. Stephan Hüfner, Photoelectron spectroscopy: principles and applications, Springer Science & Business Media2013.

57. Xin Sun, Yi Jin, Chen-Yu Zhang, Jian-Wu Wen, Yu Shao, Yong Zang, Chun-Hua Chen, *"$Na[Ni_{0.4}Fe_{0.2}Mn_{0.4-x}Ti_x]O_2$: a cathode of high capacity and superior cyclability for Na-ion batteries"*, **Journal of Materials Chemistry A** 2(41) (2014) 17268-17271. https://doi.org/10.1039/C4TA03828B.

58. Peng-Fei Wang, Ya You, Ya-Xia Yin, Yue-Sheng Wang, Li-Jun Wan, Lin Gu, Yu-Guo Guo, *"Suppressing the P2–O2 Phase Transition of $Na_{0.67}Mn_{0.67}Ni_{0.33}O_2$ by Magnesium Substitution for Improved Sodium-Ion Batteries"*, **Angewandte Chemie International Edition** 55(26) (2016) 7445-7449. https://doi.org/10.1002/anie.201602202.

59. Xuehang Wu, Gui-Liang Xu, Guiming Zhong, Zhengliang Gong, Matthew J. McDonald, Shiyao Zheng, Riqiang Fu, Zonghai Chen, Khalil Amine, Yong Yang, *"Insights into the Effects of Zinc Doping on Structural Phase Transition of P2-Type Sodium Nickel Manganese Oxide Cathodes for High-Energy Sodium Ion Batteries"*, **ACS Applied Materials & Interfaces** 8(34) (2016) 22227-22237. https://doi.org/10.1021/acsami.6b06701.

60. Naoaki Yabuuchi, Masataka Kajiyama, Junichi Iwatate, Heisuke Nishikawa, Shuji Hitomi, Ryoichi Okuyama, Ryo Usui, Yasuhiro Yamada, Shinichi Komaba, *"P2-type $Na_x[Fe_{1/2}Mn_{1/2}]O_2$ made from earth-abundant elements for rechargeable Na batteries"*, **Nature Materials** 11(6) (2012) 512-517. https://doi.org/10.1038/nmat3309.

61. Duho Kim, Maenghyo Cho, Kyeongjae Cho, *"Rational Design of $Na(Li_{1/3}Mn_{2/3})O_2$ Operated by Anionic Redox Reactions for Advanced Sodium-Ion Batteries"*, **Advanced Materials** 29(33) (2017) 1701788. https://doi.org/10.1002/adma.201701788.

62. Xiaohui Rong, Enyuan Hu, Yaxiang Lu, Fanqi Meng, Chenglong Zhao, Xuelong Wang, Qinghua Zhang, Xiqian Yu, Lin Gu, Yong-Sheng Hu, Hong Li, Xuejie Huang, Xiao-Qing Yang, Claude Delmas, Liquan Chen, *"Anionic Redox Reaction-Induced High-Capacity and Low-Strain Cathode with Suppressed Phase Transition"*, **Joule** 3(2) (2019) 503-517. https://doi.org/10.1016/j.joule.2018.10.022.

63. Yong Li, Guoliang Liu, Jiangxuan Che, Liping Chen, Xuan Wang, Guangming Wang, Lanlan Lei, Jie Hou, Shuyue Li, Juan Wang, Yunhua Xu, Yufeng Zhao, *"Review on layered oxide cathodes for sodium-ion batteries: Degradation mechanisms, modification strategies, and applications"*, **Interdisciplinary Materials** n/a(n/a). https://doi.org/10.1002/idm2.12213.

64. W. Weppner, R. A. Huggins, *"Determination of the Kinetic Parameters of Mixed-Conducting Electrodes and Application to the System Li_3Sb"*, **Journal of the Electrochemical Society** 124(10) (1977) 1569. https://doi.org/10.1149/1.2133112.

65. Yonglin Tang, Qinghua Zhang, Wenhua Zuo, Shiyuan Zhou, Guifan Zeng, Baodan Zhang, Haitang Zhang, Zhongyuan Huang, Lirong Zheng, Juping Xu, Wen Yin, Yongfu Qiu, Yinguo Xiao, Qiaobao Zhang, Tiqing Zhao, Hong-Gang Liao, Inhui Hwang, Cheng-Jun Sun, Khalil Amine, Qingsong Wang, Yang Sun, Gui-Liang Xu, Lin Gu, Yu Qiao, Shi-Gang Sun, *"Sustainable layered cathode with suppressed phase transition for long-life sodium-ion*

batteries", **Nature Sustainability** 7(3) (2024) 348-359. https://doi.org/10.1038/s41893-024-01288-9.

66. Xiaotong Wang, Qinghua Zhang, Chen Zhao, Haifeng Li, Baodan Zhang, Guifan Zeng, Yonglin Tang, Zhongyuan Huang, Inhui Hwang, Haitang Zhang, Shiyuan Zhou, Yongfu Qiu, Yinguo Xiao, Jordi Cabana, Cheng-Jun Sun, Khalil Amine, Yang Sun, Qingsong Wang, Gui-Liang Xu, Lin Gu, Yu Qiao, Shi-Gang Sun, *"Achieving a high-performance sodium-ion pouch cell by regulating intergrowth structures in a layered oxide cathode with anionic redox"*, **Nature Energy** 9(2) (2024) 184-196. https://doi.org/10.1038/s41560-023-01425-2.

67. Kai Fang, Jianhua Yin, Guifan Zeng, Zixin Wu, Yonglin Tang, Dongyan Yu, Haiyan Luo, Qirui Liu, Qinghua Zhang, Tian Qiu, Huan Huang, Ziyang Ning, Chuying Ouyang, Lin Gu, Yu Qiao, Shi-Gang Sun, *"Elucidating the Structural Evolution of O3-type* $NaNi_{1/3}Fe_{1/3}Mn_{1/3}O_2$*: A Prototype Cathode for Na-Ion Battery"*, **Journal of the American Chemical Society** 146(46) (2024) 31860-31872. https://doi.org/10.1021/jacs.4c11049.

68. Ying Yang, Yuzhang Feng, Zhuo Chen, Yiming Feng, Qun Huang, Cheng Ma, Qingbing Xia, Chaoping Liang, Liangjun Zhou, M. Saiful Islam, Peng Wang, Liang Zhou, Liqiang Mai, Weifeng Wei, *"Strain engineering by atomic lattice locking in P2-type layered oxide cathode for high-voltage sodium-ion batteries"*, **Nano Energy** 76 (2020) 105061. https://doi.org/10.1016/j.nanoen.2020.105061.

69. Zhengbo Liu, Jiadong Shen, Shihui Feng, Yalan Huang, Duojie Wu, Fangkun Li, Yuanmin Zhu, Meng Gu, Qi Liu, Jun Liu, Min Zhu, *"Ultralow Volume Change of P2-Type Layered Oxide Cathode for Na-Ion Batteries with Controlled Phase Transition by Regulating Distribution of* Na^+*"*, **Angewandte Chemie International Edition** 60(38) (2021) 20960-20969. https://doi.org/10.1002/anie.202108109.

70. Wenhua Zuo, Xiangsi Liu, Jimin Qiu, Dexin Zhang, Zhumei Xiao, Jisheng Xie, Fucheng Ren, Jinming Wang, Yixiao Li, Gregorio F. Ortiz, Wen Wen, Shunqing Wu, Ming-Sheng Wang, Riqiang Fu, Yong Yang, *"Engineering* Na^+*-layer spacings to stabilize Mn-based layered cathodes for sodium-ion batteries"*, **Nature Communications** 12(1) (2021) 4903. https://doi.org/10.1038/s41467-021-25074-9.

Supplementary material (SI)

Strategic Phase Modulation in $Na_{0.8}(Mn\text{-}Fe\text{-}Ni)O_2$ System Delivers High Energy Density and Structural Stability

Samriddhi Saxena [a], Hari Narayanan Vasavan [a], Neha Dagar [a], Velaga Srihari [b], Asish Kumar Das [a], Pratiksha Gami [a], Sonia Deswal [c], Pradeep Kumar [c], Himanshu Kumar Poswal [b], Sunil Kumar [a,*]

[a] *Department of Metallurgical Engineering and Materials Science, Indian Institute of Technology Indore, Simrol, 453552, India*

[b] *High Pressure & Synchrotron Radiation Physics Division, Bhabha Atomic Research Centre, Mumbai 400085, India*

[c] *School of Physical Sciences, Indian Institute of Technology Mandi, Mandi, 175005, India*

[*] *E-mail: sunil@iiti.ac.in*

Table S1 Fractions (in %) of P3, P2, and O3 phases at different calcination temperatures in MFN samples.

Calcination Temperature	**700 °C**			**800 °C**			**900 °C**			**1000 °C**		
Composition	**P3**	**P2**	**O3**	**P3**	**P2**	**O3**	**P3**	**P2**	**O3**	**P3**	**P2**	**O3**
MFN-A	46 ± 3	-	54 ± 3	-	67 ± 1	33 ± 1	-	84 ± 2	16 ± 2	-	100	-
MFN-B	49 ± 3	51 ± 3	-	-	100	-	-	100	-	-	100	-
MFN-C	67 ± 2	-	33 ± 2	22 ± 4	39 ± 4	39 ± 4	-	64 ± 2	36 ± 2	-	37 ± 2	59 ± 2
MFN-D	74 ± 3	26 ± 3	-	-	100	-	-	100	-	-	100	-
MFN-E	23 ± 1	75 ± 1	2 ± 1	-	98 ± 1	2 ± 1	-	98 ± 1	2 ± 1	-	100	-
MFN-F	72 ± 1	26 ± 1	2 ± 1	18 ± 7	77 ± 2	5 ± 2	-	95 ± 2	5 ± 2	-	100	-
MFN-G	64 ± 1	34 ± 1	2 ± 1	-	98 ± 1	2 ± 1	-	98 ± 1	2 ± 1	-	100	-

Table S2 Lattice parameters of the MFN samples calcined at 700 °C obtained from the Rietveld refinement of XRD data.

Sample	***a* (Å)**	***c* (Å)**	***V* (Å^3)**	**R_{wp}, R_{exp}, R_p, *GOF***
MFN-A	2.8987 ± 0.0002	16.772 ± 0.001	122.05 ± 0.02	3.62, 3.20, 2.87, 1.13
	2.9407 ± 0.0001	16.434 ± 0.001	123.08 ± 0.01	
MFN-B	2.9092 ± 0.0006	16.733 ± 0.003	122.65 ± 0.06	3.78, 3.21, 2.94, 1.17
	2.9011 ± 0.0005	11.168 ± 0.001	81.40 ± 0.03	
MFN-C	2.8958 ± 0.0002	16.757 ± 0.002	121.69 ± 0.02	4.33, 3.78, 3.44, 1.14
	2.9553 ± 0.0003	16.192 ± 0.002	122.479 ± 0.035	
MFN-D	2.8955 ± 0.0002	16.798 ± 0.001	121.96 ± 0.02	2.91, 2.47, 2.29, 1.17
	2.8978 ± 0.0002	11.172 ± 0.001	81.25 ± 0.01	
MFN-E	2.8945 ± 0.0004	16.651 ± 0.001	120.82 ± 0.04	4.40, 3.48, 3.43, 1.26
	2.8944 ± 0.0001	11.1462 ± 0.0007	80.872 ± 0.008	
	2.8889 ± 0.0004	15.984 ± 0.003	115.53 ± 0.04	
MFN-F	2.8923 ± 0.0001	16.767 ± 0.001	121.47 ± 0.01	3.55, 2.72, 2.68, 1.30
	2.8916 ± 0.0001	11.178 ± 0.006	80.94 ± 0.04	
	2.953 ± 0.001	16.063 ± 0.005	121.35 ± 0.09	

MFN-G	2.8901 ± 0.0001	16.786 ± 0.001	121.43 ± 0.01	3.08, 2.58, 2.40, 1.19
	2.8905 ± 0.0001	11.143 ± 0.002	80.63 ± 0.01	
	2.8863 ± 0.0003	16.026 ± 0.002	115.63 ± 0.03	

Table S3 Lattice parameters of the MFN samples calcined at 800°C obtained from the Rietveld refinement of XRD data.

Sample	***a*** **(Å)**	***c*** **(Å)**	***V*** **(Å^3)**	**R_{wp}, R_{exp}, R_p, *GOF***
MFN-A	2.90893 ± 0.00003	11.1412 ± 0.0002	81.645 ± 0.002	2.68, 2.33, 2.08, 1.15
	2.94438 ± 0.00007	16.3830 ± 0.0006	123.003 ± 0.008	
MFN-B	2.9018 ± 0.0002	11.1914 ± 0.0008	81.61 ± 0.01	2.72, 2.29, 2.10, 1.18
MFN-C	2.8978 ± 0.0004	16.706 ± 0.002	121.49 ± 0.03	2.99, 2.63, 2.34, 1.13
	2.90406 ± 0.00008	11.0887 ± 0.0005	80.989 ± 0.006	
	2.94791 ± 0.00009	6.220 ± 0.001	122.07 ± 0.01	
MFN-D	2.89720 ± 0.00004	11.1687 ± 0.0003	81.188 ± 0.003	3.11, 2.54, 2.38, 1.22
MFN-E	2.89772 ± 0.00008	11.1693 ± 0.0006	81.221 ± 0.007	3.31, 2.47, 2.47, 1.33
	2.8896 ± 0.0002	16.014 ± 0.002	115.80 ± 0.02	
MFN-F	2.8904 ± 0.0003	16.749 ± 0.002	121.18 ± 0.03	3.44, 2.87, 2.70, 1.19
	2.89446 ± 0.00009	11.1344 ± 0.0004	80.786 ± 0.006	

	2.9462 ± 0.0004	16.131 ± 0.004	121.26 ± 0.05	
MFN-G	2.89001 ± 0.00005	11.1466 ± 0.0004	80.626 ± 0.004	3.39, 2.75, 2.65, 1.23
	2.8910 ± 0.0004	16.019 ± 0.003	115.95 ± 0.04	

Table S4 Lattice parameters of the MFN samples calcined at 900°C obtained from the Rietveld refinement of XRD data.

Sample	***a* (Å)**	***c* (Å)**	***V* (Å^3)**	**R_{wp}, R_{exp}, R_p, *GOF***
MFN-A	2.91143 ± 0.00002	11.1338 ± 0.0001	81.732 ± 0.002	2.95, 2.27, 2.20, 1.29
	2.94614 ± 0.00008	16.3622 ± 0.0006	122.993 ± 0.008	
MFN-B	2.90624 ± 0.00008	11.1988 ± 0.0005	81.916 ± 0.007	2.71, 2.27, 2.11, 1.19
MFN-C	2.90546 ± 0.00004	11.0886 ± 0.0002	81.067 ± 0.003	3.52, 2.55, 2.62, 1.38
	2.94540 ± 0.00007	16.2314 ± 0.0007	121.949 ± 0.008	
MFN-D	2.89720 ± 0.00003	11.1773 ± 0.0002	81.251 ± 0.003	3.15, 2.50, 2.34, 1.25
MFN-E	2.90065 ± 0.00008	11.1719 ± 0.0006	81.405 ± 0.007	3.23, 2.48, 2.46, 1.30
	2.8891 ± 0.0002	16.030 ± 0.003	115.88 ± 0.03	
MFN-F	2.89362 ± 0.00004	11.1291 ± 0.0003	80.701 ± 0.004	3.82, 2.68, 2.84, 1.42
	2.9286 ± 0.0004	16.301 ± 0.004	121.08 ± 0.05	
MFN-G	2.88648 ± 0.00004	11.1614 ± 0.0004	80.535 ± 0.004	3.50, 2.62, 2.59, 1.33

	2.957 ± 0.003	16.02 ± 0.02	121.3 ± 0.3	

Table S5 Lattice parameters of the MFN samples calcined at 1000°C obtained from the Rietveld refinement of XRD data.

Sample	***a*** **(Å)**	***c*** **(Å)**	***V*** **(Å^3)**	R_{wp}, R_{exp}, R_p, ***GOF***
MFN-A	2.91124 ± 0.00002	11.1578 ± 0.0001	81.897 ± 0.002	2.38, 1.87, 1.80, 1.27
MFN-B	2.91044 ± 0.00005	11.2139 ± 0.0004	82.264 ± 0.004	2.60, 1.92, 1.93, 1.35
MFN-C	2.90599 ± 0.00005	11.1011 ± 0.0003	81.187 ± 0.004	3.68, 2.01, 2.34, 1.82
	2.93049 ± 0.00004	16.3665 ± 0.0005	121.722 ± 0.005	
	4.1865 ± 0.0003	-	73.38 ± 0.02	
MFN-D	2.89854 ± 0.00003	11.1777 ± 0.0002	81.329 ± 0.003	2.62, 2.04, 1.97, 1.28
MFN-E	2.90205 ± 0.00007	11.1968 ± 0.0006	81.665 ± 0.006	2.28, 1.94, 1.76, 1.17
MFN-F	2.89366 ± 0.00005	11.1389 ± 0.0004	80.767 ± 0.004	2.98, 2.28, 2.28, 1.30
MFN-G	2.88877 ± 0.00008	11.1701 ± 0.0005	80.727 ± 0.006	3.08, 2.14, 2.22, 1.44

Tables S6-S33 Crystallographic parameters of MFN samples calcined at different temperatures obtained from Rietveld refinement of room temperature XRD data.

S6: MFN-A-700

P3 (Space Group: R3m)

Atom	x	y	z	Occupancy	Site
Na	0	0	0.17	0.8	3a
Mn/Fe/Ni	0	0	0	0.53/0.25/0.22	3a
O1	0	0	0.396±0.002	1.00	3a
O2	0	0	0.604±0.002	1.00	3a

O3 (Space Group: $R\bar{3}m$)

Atom	x	y	z	Occupancy	Site
Na1	0	0	½	0.8	3b
Mn/Fe/Ni	0	0	0	0.53/0.25/0.22	3a
O	0	0	0.269±0.001	1	6c

S7: MFN-B-700

P3 (Space Group: R3m)

Atom	x	y	z	Occupancy	Site
Na	0	0	0.17	0.8	3a
Mn/Fe/Ni	0	0	0	0.64/0.25/0.11	3a
O1	0	0	0.402±0.004	1.00	3a
O2	0	0	0.598±0.004	1.00	3a

P2 (Space Group : $P6_3/mmc$)

Atom	x	y	z	Occupancy	Site
Na1	2/3	1/3	1/4	0.5	2d
Na2	0	0	1/4	0.3	2b
Mn/Fe/Ni	0	0	0	0.64/0.25/0.11	2a
O	2/3	1/3	0.095±0.001	1	4f

S8: MFN-C-700

P3 (Space Group: R3m)

Atom	x	y	z	Occupancy	Site
Na	0	0	0.17	0.8	3a

Mn/Fe/Ni	0	0	0	0.53/0.14/0.33	3a
O1	0	0	0.397±0.003	1.00	3a
O2	0	0	0.603±0.003	1.00	3a
O3 (Space Group: $R\bar{3}m$)					
Atom	**x**	**y**	**z**	**Occupancy**	**Site**
Na1	0	0	½	0.8	3b
Mn/Fe/Ni	0	0	0	0.53/0.14/0.33	3a
O	0	0	0.274±0.005	1	6c
S9: MFN-D-700					
P3 (Space Group: R3m)					
Atom	**x**	**y**	**z**	**Occupancy**	**Site**
Na	0	0	0.17	0.8	3a
Mn/Fe/Ni	0	0	0	0.64/0.14/0.22	3a
O1	0	0	0.399±0.002	1.00	3a
O2	0	0	0.601±0.002	1.00	3a
P2 (Space Group : $P6_3/mmc$)					
Atom	**x**	**y**	**z**	**Occupancy**	**Site**
Na1	2/3	1/3	1/4	0.5	2d
Na2	0	0	1/4	0.3	2b
Mn/Fe/Ni	0	0	0	0.64/0.14/0.22	2a
O	2/3	1/3	0.097±0.002	1	4f
S10: MFN-E-700					
P3 (Space Group: R3m)					
Atom	**x**	**y**	**z**	**Occupancy**	**Site**
Na	0	0	0.17	0.8	3a
Mn/Fe/Ni	0	0	0	0.75/0.14/0.11	3a
O1	0	0	0.400±0.005	1.00	3a
O2	0	0	0.600±0.005	1.00	3a
P2 (Space Group : $P6_3/mmc$)					
Atom	**x**	**y**	**z**	**Occupancy**	**Site**
Na1	2/3	1/3	1/4	0.5	2d

Na2	0	0	1/4	0.3	2b
Mn/Fe/Ni	0	0	0	0.75/0.14/0.11	2a
O	2/3	1/3	0.098±0.001	1	4f

O3 (Space Group: $R\bar{3}m$)

Atom	**x**	**y**	**z**	**Occupancy**	**Site**
Na1	0	0	½	0.8	3b
Mn/Fe/Ni	0	0	0	0.75/0.14/0.11	3a
O	0	0	0.299±0.003	1	6c

S11: MFN-F-700

P3 (Space Group: R3m)

Atom	**x**	**y**	**z**	**Occupancy**	**Site**
Na	0	0	0.17	0.8	3a
Mn/Fe/Ni	0	0	0	0.64/0.03/0.33	3a
O1	0	0	0.400±0.004	1.00	3a
O2	0	0	0.600±0.004	1.00	3a

P2 (Space Group : $P6_3/mmc$)

Atom	**x**	**y**	**z**	**Occupancy**	**Site**
Na1	2/3	1/3	1/4	0.5	2d
Na2	0	0	1/4	0.3	2b
Mn/Fe/Ni	0	0	0	0.64/0.03/0.33	2a
O	2/3	1/3	0.092±0.002	1	4f

O3 (Space Group: $R\bar{3}m$)

Atom	**x**	**y**	**z**	**Occupancy**	**Site**
Na1	0	0	½	0.8	3b
Mn/Fe/Ni	0	0	0	0.64/0.03/0.33	3a
O	0	0	0.274±0.004	1	6c

S12: MFN-G-700

P3 (Space Group: R3m)

Atom	**x**	**y**	**z**	**Occupancy**	**Site**
Na	0	0	0.17	0.8	3a
Mn/Fe/Ni	0	0	0	0.75/0.03/0.22	3a

O1	0	0	0.401±0.004	1.00	3a
O2	0	0	0.599±0.004	1.00	3a

P2 (Space Group : $P6_3/mmc$)

Atom	**x**	**y**	**z**	**Occupancy**	**Site**
Na1	2/3	1/3	1/4	0.5	2d
Na2	0	0	1/4	0.3	2b
Mn/Fe/Ni	0	0	0	0.75/0.03/0.22	2a
O	2/3	1/3	0.093±0.002	1	4f

O3 (Space Group: $R\bar{3}m$)

Atom	**x**	**y**	**z**	**Occupancy**	**Site**
Na1	0	0	½	0.8	3b
Mn/Fe/Ni	0	0	0	0.75/0.03/0.22	3a
O	0	0	0.256±0.004	1	6c

S13: MFN-A-800

O3 (Space Group: $R\bar{3}m$)

Atom	**x**	**y**	**Z**	**Occupancy**	**Site**
Na1	0	0	½	0.8	3b
Mn/Fe/Ni	0	0	0	0.53/0.25/0.22	3a
O	0	0	0.269±0.002	1	6c

P2 (Space Group : $P6_3/mmc$)

Atom	**x**	**y**	**Z**	**Occupancy**	**Site**
Na1	2/3	1/3	¼	0.5	2d
Na2	0	0	¼	0.3	2b
Mn/Fe/Ni	0	0	0	0.53/0.25/0.22	2a
O	2/3	1/3	0.096±0.001	1	4f

S14: MFN-B-800

P2 (Space Group : $P6_3/mmc$)

Atom	**x**	**y**	**Z**	**Occupancy**	**Site**
Na1	2/3	1/3	¼	0.5	2d
Na2	0	0	¼	0.3	2b

Mn/Fe/Ni	0	0	0	0.64/0.25/0.11	2a
O	2/3	1/3	0.098±0.001	1	4f
S15: MFN-C-800					
P3 (Space Group: R3m)					
Atom	**x**	**y**	**Z**	**Occupancy**	**Site**
Na	0	0	0.17	0.8	3a
Mn/Fe/Ni	0	0	0	0.53/0.14/0.33	3a
O1	0	0	0.397±0.003	1.00	3a
O2	0	0	0.603±0.003	1.00	3a
O3 (Space Group: $R\bar{3}m$)					
Atom	**x**	**y**	**Z**	**Occupancy**	**Site**
Na1	0	0	½	0.8	3b
Mn/Fe/Ni	0	0	0	0.53/0.14/0.33	3a
O	0	0	0.274±0.005	1	6c
P2 (Space Group : $P6_3/mmc$)					
Atom	**x**	**y**	**Z**	**Occupancy**	**Site**
Na1	2/3	1/3	¼	0.5	2d
Na2	0	0	¼	0.3	2b
Mn/Fe/Ni	0	0	0	0.53/0.14/0.33	2a
O	2/3	1/3	0.094±0.001	1	4f
S16: MFN-D-800					
P2 (Space Group : $P6_3/mmc$)					
Atom	**x**	**y**	**Z**	**Occupancy**	**Site**
Na1	2/3	1/3	¼	0.5	2d
Na2	0	0	¼	0.3	2b
Mn/Fe/Ni	0	0	0	0.64/0.14/0.22	2a
O	2/3	1/3	0.099±0.001	1	4f
S17: MFN-E-800					
P2 (Space Group : $P6_3/mmc$)					
Atom	**x**	**y**	**Z**	**Occupancy**	**Site**
Na1	2/3	1/3	¼	0.5	2d

Na2	0	0	¼	0.3	2b
Mn/Fe/Ni	0	0	0	0.75/0.14/0.11	2a
O	2/3	1/3	0.099±0.001	1	4f
O3 (Space Group: $R\bar{3}m$)					
Atom	**x**	**y**	**Z**	**Occupancy**	**Site**
Na1	0	0	½	0.8	3b
Mn/Fe/Ni	0	0	0	0.75/0.14/0.11	3a
O	0	0	0.27±0.02	1	6c
S18: MFN-F-800					
P3 (Space Group: $R3m$)					
Atom	**x**	**y**	**Z**	**Occupancy**	**Site**
Na	0	0	0.17	0.8	3a
Mn/Fe/Ni	0	0	0	0.64/0.03/0.33	3a
O1	0	0	0.400±0.006	1.00	3a
O2	0	0	0.600±0.006	1.00	3a
P2 (Space Group : $P6_3/mmc$)					
Atom	**x**	**y**	**Z**	**Occupancy**	**Site**
Na1	2/3	1/3	¼	0.5	2d
Na2	0	0	¼	0.3	2b
Mn/Fe/Ni	0	0	0	0.64/0.03/0.33	2a
O	2/3	1/3	0.096±0.001	1	4f
O3 (Space Group: $R\bar{3}m$)					
Atom	**x**	**y**	**Z**	**Occupancy**	**Site**
Na1	0	0	½	0.8	3b
Mn/Fe/Ni	0	0	0	0.64/0.03/0.33	3a
O	0	0	0.271±0.001	1	6c
S19: MFN-G-800					
P2 (Space Group : $P6_3/mmc$)					
Atom	**x**	**y**	**Z**	**Occupancy**	**Site**
Na1	2/3	1/3	¼	0.5	2d
Na2	0	0	¼	0.3	2b

Mn/Fe/Ni	0	0	0	0.75/0.03/0.22	2a
O	2/3	1/3	0.097±0.001	1	4f

O3 (Space Group: $R\bar{3}m$)

Atom	x	y	Z	Occupancy	Site
Na1	0	0	½	0.8	3b
Mn/Fe/Ni	0	0	0	0.75/0.03/0.22	3a
O	0	0	0.27±0.05	1	6c

S20: MFN-A-900

O3 (Space Group: $R\bar{3}m$)

Atom	x	y	Z	Occupancy	Site
Na1	0	0	½	0.8	3b
Mn/Fe/Ni	0	0	0	0.53/0.25/0.22	3a
O	0	0	0.269±0.001	1	6c

P2 (Space Group : $P6_3/mmc$)

Atom	x	y	Z	Occupancy	Site
Na1	2/3	1/3	¼	0.5	2d
Na2	0	0	¼	0.3	2b
Mn/Fe/Ni	0	0	0	0.53/0.25/0.22	2a
O	2/3	1/3	0.095±0.001	1	4f

S21: MFN-B-900

P2 (Space Group : $P6_3/mmc$)

Atom	x	y	Z	Occupancy	Site
Na1	2/3	1/3	¼	0.5	2d
Na2	0	0	¼	0.3	2b
Mn/Fe/Ni	0	0	0	0.64/0.25/0.11	2a
O	2/3	1/3	0.098±0.001	1	4f

S22: MFN-C-900

O3 (Space Group: $R\bar{3}m$)

Atom	x	y	Z	Occupancy	Site
Na1	0	0	½	0.8	3b

Mn/Fe/Ni	0	0	0	0.53/0.14/0.33	3a
O	0	0	0.270±0.001	1	6c
P2 (Space Group : $P6_3/mmc$)					
Atom	**x**	**y**	**Z**	**Occupancy**	**Site**
Na1	2/3	1/3	¼	0.5	2d
Na2	0	0	¼	0.3	2b
Mn/Fe/Ni	0	0	0	0.53/0.14/0.33	2a
O	2/3	1/3	0.094±0.001	1	4f
S23: MFN-D-900					
P2 (Space Group : $P6_3/mmc$)					
Atom	**x**	**y**	**Z**	**Occupancy**	**Site**
Na1	2/3	1/3	¼	0.5	2d
Na2	0	0	¼	0.3	2b
Mn/Fe/Ni	0	0	0	0.64/0.14/0.22	2a
O	2/3	1/3	0.098±0.001	1	4f
S24: MFN-E-900					
P2 (Space Group : $P6_3/mmc$)					
Atom	**x**	**y**	**Z**	**Occupancy**	**Site**
Na1	2/3	1/3	¼	0.5	2d
Na2	0	0	¼	0.3	2b
Mn/Fe/Ni	0	0	0	0.75/0.14/0.11	2a
O	2/3	1/3	0.099±0.001	1	4f
O3 (Space Group: $R\bar{3}m$)					
Atom	**x**	**y**	**Z**	**Occupancy**	**Site**
Na1	0	0	½	0.8	3b
Mn/Fe/Ni	0	0	0	0.75/0.14/0.11	3a
O	0	0	0.31±0.01	1	6c
S25: MFN-F-900					
P2 (Space Group : $P6_3/mmc$)					
Atom	**x**	**y**	**Z**	**Occupancy**	**Site**
Na1	2/3	1/3	¼	0.5	2d

Na2	0	0	¼	0.3	2b
Mn/Fe/Ni	0	0	0	0.64/0.03/0.33	2a
O	2/3	1/3	0.097±0.001	1	4f

O3 (Space Group: $R\bar{3}m$)

Atom	**x**	**y**	**Z**	**Occupancy**	**Site**
Na1	0	0	½	0.8	3b
Mn/Fe/Ni	0	0	0	0.64/0.03/0.33	3a
O	0	0	0.27±0.02	1	6c

S26: MFN-G-900

P2 (Space Group : $P6_3/mmc$)

Atom	**x**	**y**	**Z**	**Occupancy**	**Site**
Na1	2/3	1/3	¼	0.5	2d
Na2	0	0	¼	0.3	2b
Mn/Fe/Ni	0	0	0	0.75/0.03/0.22	2a
O	2/3	1/3	0.099±0.001	1	4f

O3 (Space Group: $R\bar{3}m$)

Atom	**x**	**y**	**Z**	**Occupancy**	**Site**
Na1	0	0	½	0.8	3b
Mn/Fe/Ni	0	0	0	0.75/0.03/0.22	3a
O	0	0	0.23±0.01	1	6c

S27: MFN-A-1000

P2 (Space Group : $P6_3/mmc$)

Atom	**x**	**y**	**Z**	**Occupancy**	**Site**
Na1	2/3	1/3	¼	0.5	2d
Na2	0	0	¼	0.3	2b
Mn/Fe/Ni	0	0	0	0.53/0.25/0.22	2a
O	2/3	1/3	0.096±0.001	1	4f

S28: MFN-B-1000

P2 (Space Group : $P6_3/mmc$)

Atom	**x**	**y**	**Z**	**Occupancy**	**Site**

Na1	2/3	1/3	¼	0.5	2d
Na2	0	0	¼	0.3	2b
Mn/Fe/Ni	0	0	0	0.64/0.25/0.11	2a
O	2/3	1/3	0.098±0.001	1	4f

S29: MFN-C-1000

O3 (Space Group: $R\bar{3}m$)

Atom	x	y	Z	Occupancy	Site
Na1	0	0	½	0.8	3b
Mn/Fe/Ni	0	0	0	0.53/0.14/0.33	3a
O	0	0	0.270±0.001	1	6c

P2 (Space Group : $P6_3/mmc$)

Atom	x	y	Z	Occupancy	Site
Na1	2/3	1/3	¼	0.5	2d
Na2	0	0	¼	0.3	2b
Mn/Fe/Ni	0	0	0	0.53/0.14/0.33	2a
O	2/3	1/3	0.098±0.001	1	4f

S30: MFN-D-1000

P2 (Space Group : $P6_3/mmc$)

Atom	x	y	z	Occupancy	Site
Na1	2/3	1/3	1/4	0.5	2d
Na2	0	0	1/4	0.3	2b
Mn/Fe/Ni	0	0	0	0.64/0.14/0.22	2a
O	2/3	1/3	0.098±0.001	1	4f

S31: MFN-E-1000

P2 (Space Group : $P6_3/mmc$)

Atom	x	y	Z	Occupancy	Site
Na1	2/3	1/3	¼	0.5	2d
Na2	0	0	¼	0.3	2b
Mn/Fe/Ni	0	0	0	0.75/0.14/0.11	2a
O	2/3	1/3	0.099±0.001	1	4f

S32: MFN-F-1000

P2 (Space Group : $P6_3/mmc$)

Atom	**x**	**y**	**z**	**Occupancy**	**Site**
Na1	2/3	1/3	1/4	0.5	2d
Na2	0	0	1/4	0.3	2b
Mn/Fe/Ni	0	0	0	0.64/0.03/0.33	2a
O	2/3	1/3	0.099±0.001	1	4f

S33: MFN-G-1000

P2 (Space Group : $P6_3/mmc$)

Atom	**x**	**y**	**z**	**Occupancy**	**Site**
Na1	2/3	1/3	1/4	0.5	2d
Na2	0	0	1/4	0.3	2b
Mn/Fe/Ni	0	0	0	0.75/0.03/0.22	2a
O	2/3	1/3	0.099±0.001	1	4f

Table S34 A comparison of the electrochemical performance of MFN samples calcined at 700 ℃.

Sample	Specific Capacity at 0.1C (mAh g^{-1})	Average voltage (V)	Capacity retention at 0.2C (of the capacity at 0.1C) (%)	Capacity retention at 1C (of the capacity at 0.1C) (%)	Capacity retention (%) after 50 cycles
MFN-A	132.7	3.44	90	69	86.5
MFN-D	124.5	3.58	93	74	89.6
MFN-C	121.6	3.39	95	73	83.4
MFN-B	114.2	3.51	85	62	82.5
MFN-G	110.4	3.49	91	51	84.2
MFN-F	96.2	3.48	90	60	80.4
MFN-E	90.1	3.42	83	71	90.7

Table S35 A comparison of the electrochemical performance of MFN samples calcined at 800 °C.

Sample	Specific Capacity at 0.1C (mAh g^{-1})	Average voltage (V)	Capacity retention at 0.2C (of the capacity at 0.1C) (%)	Capacity retention at 1C (of the capacity at 0.1C) (%)	Capacity retention (%) after 50 cycles
MFN-A	134.2	3.48	90	66	87.6
MFN-C	131.9	3.40	94	72	76.7
MFN-D	127.3	3.60	92	67	88.3
MFN-B	109.6	3.45	82	56	77.8
MFN-F	113.3	3.51	89	64	75.2
MFN-G	94.7	3.54	91	63	81.4
MFN-E	89.7	3.42	87	63	80.7

Table S36 A comparison of the electrochemical performance of MFN samples calcined at 900 °C.

Sample	Specific Capacity at 0.1C (mAh g^{-1})	Average voltage (V)	Capacity retention at 0.2C (of the capacity at 0.1C) (%)	Capacity retention at 1C (of the capacity at 0.1C) (%)	Capacity retention (%) after 50 cycles
MFN-C	139.1	3.50	83	52	72.2
MFN-A	120.7	3.49	83	37	80.0
MFN-D	119.9	3.56	81	43	89.7
MFN-F	110.8	3.57	84	37	53.8
MFN-B	108.8	3.57	77	36	85.5
MFN-G	107.5	3.63	82	39	78.4
MFN-E	89.1	3.37	73	31	83.1

Table S37 A comparison of the electrochemical performance of MFN samples calcined at 1000°C.

Sample	Specific Capacity at 0.1C (mAh g^{-1})	Average voltage (V)	Capacity retention at 0.2C (of the capacity at 0.1C) (%)	Capacity retention at 1C (of the capacity at 0.1C) (%)	Capacity retention (%) after 50 cycles
MFN-C	126.7	3.26	63	25	36.7
MFN-A	123.1	3.51	71	25	71.9
MFN-D	121.1	3.56	80	30	52.0
MFN-F	111.1	3.53	79	25	22.7
MFN-G	96.4	3.69	70	32	61.8
MFN-E	84.7	3.25	78	28	35.8
MFN-B	79.6	3.36	58	10	21.7

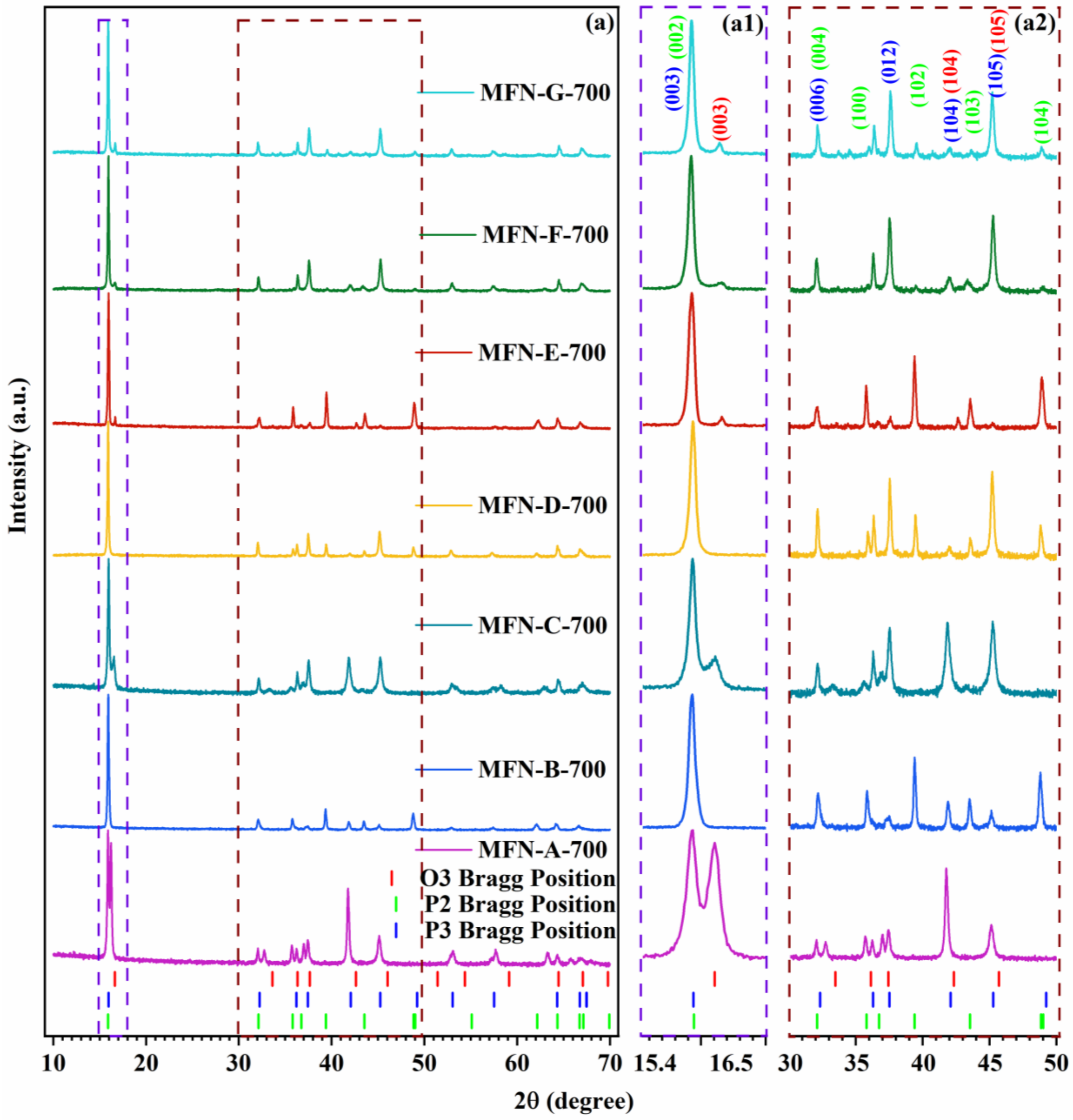

Fig. S1. (a) XRD patterns of the MFN samples calcined at 700 °C. (a1) and (a2) Magnified view of the characteristic peaks of P3, P2, and O3 phases.

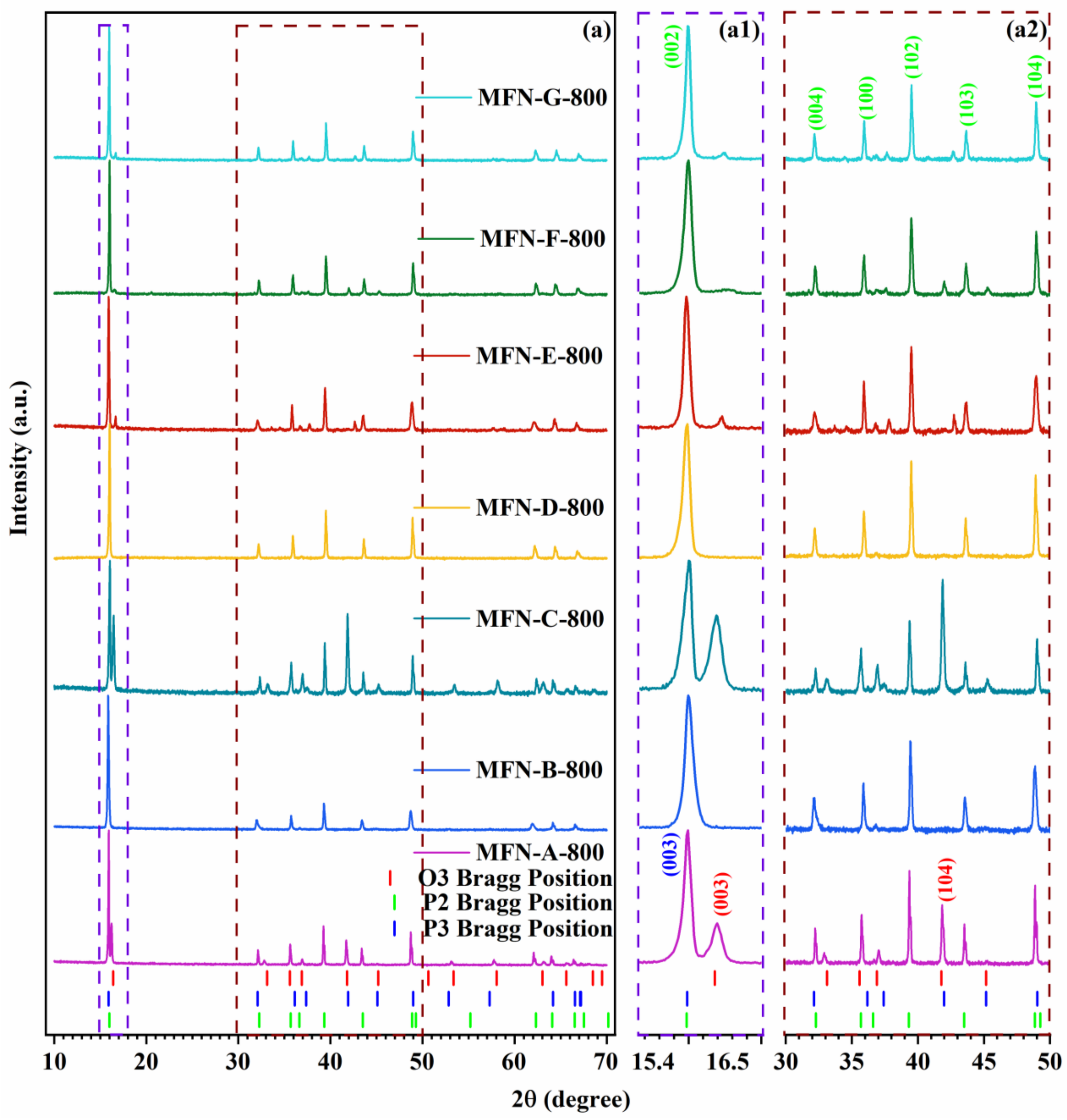

Fig. S2. (a) XRD patterns of the MFN samples calcined at 800 °C. (a1) and (a2) Magnified view of the characteristic peaks of P3, P2, and O3 phases.

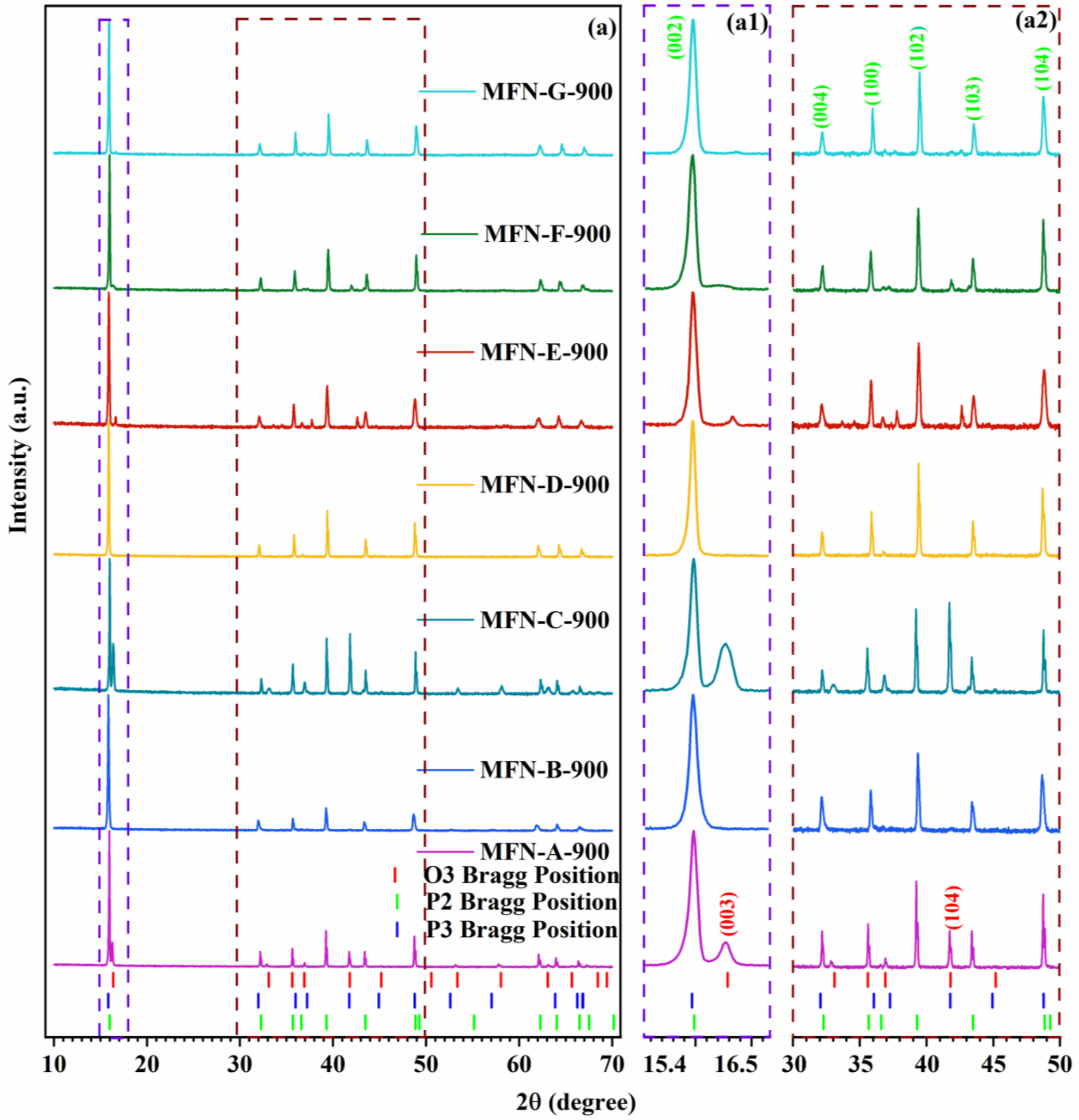

Fig. S3. (a) XRD patterns of the MFN samples calcined at 900°C. (a1) and (a2) Magnified view of the characteristic peaks of P2 and O3 phases.

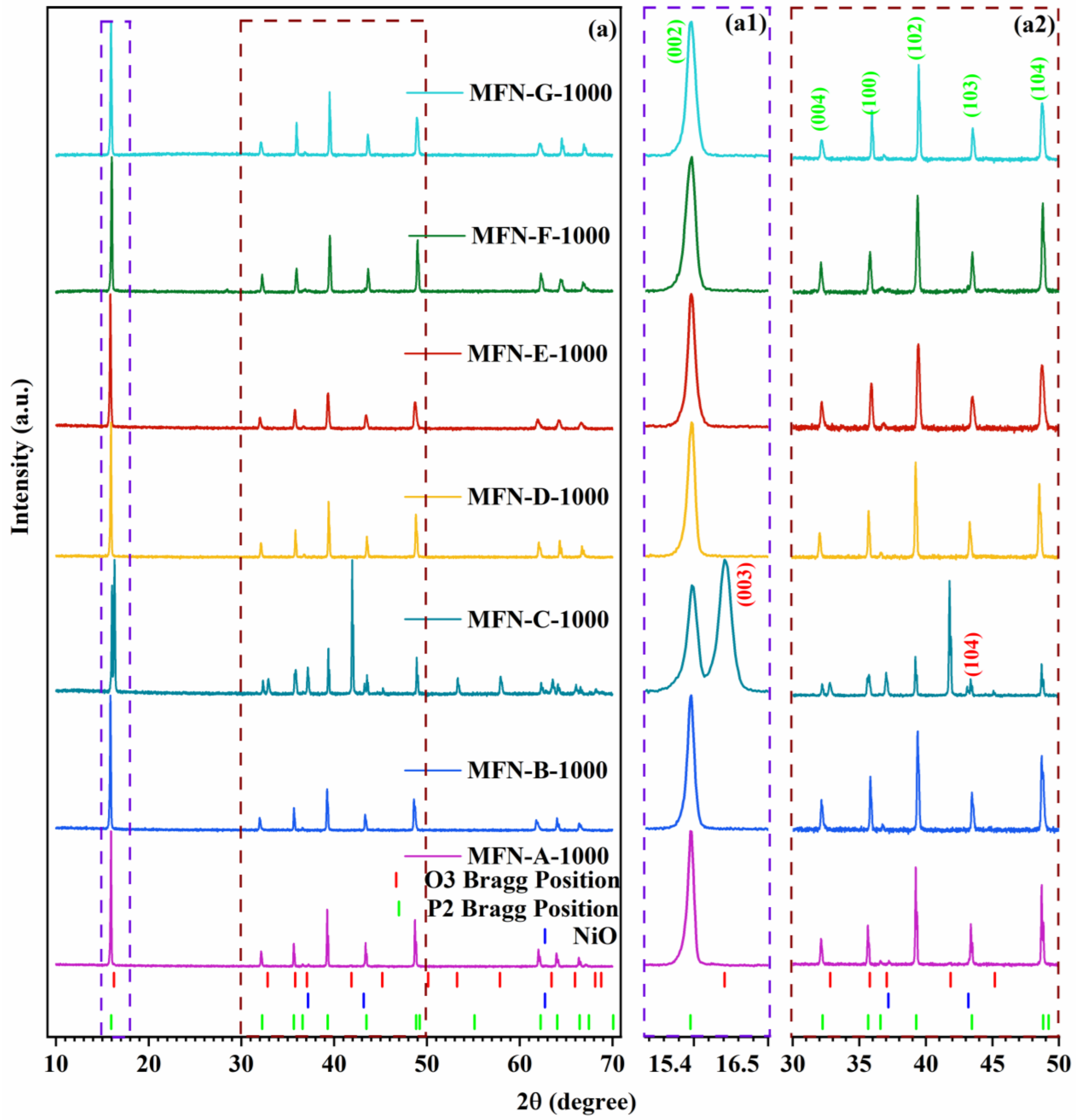

Fig. S4. (a) XRD patterns of the MFN samples calcined at 1000 °C. (a1) and (a2) Magnified view of the characteristic peaks of P2 and O3 phases.

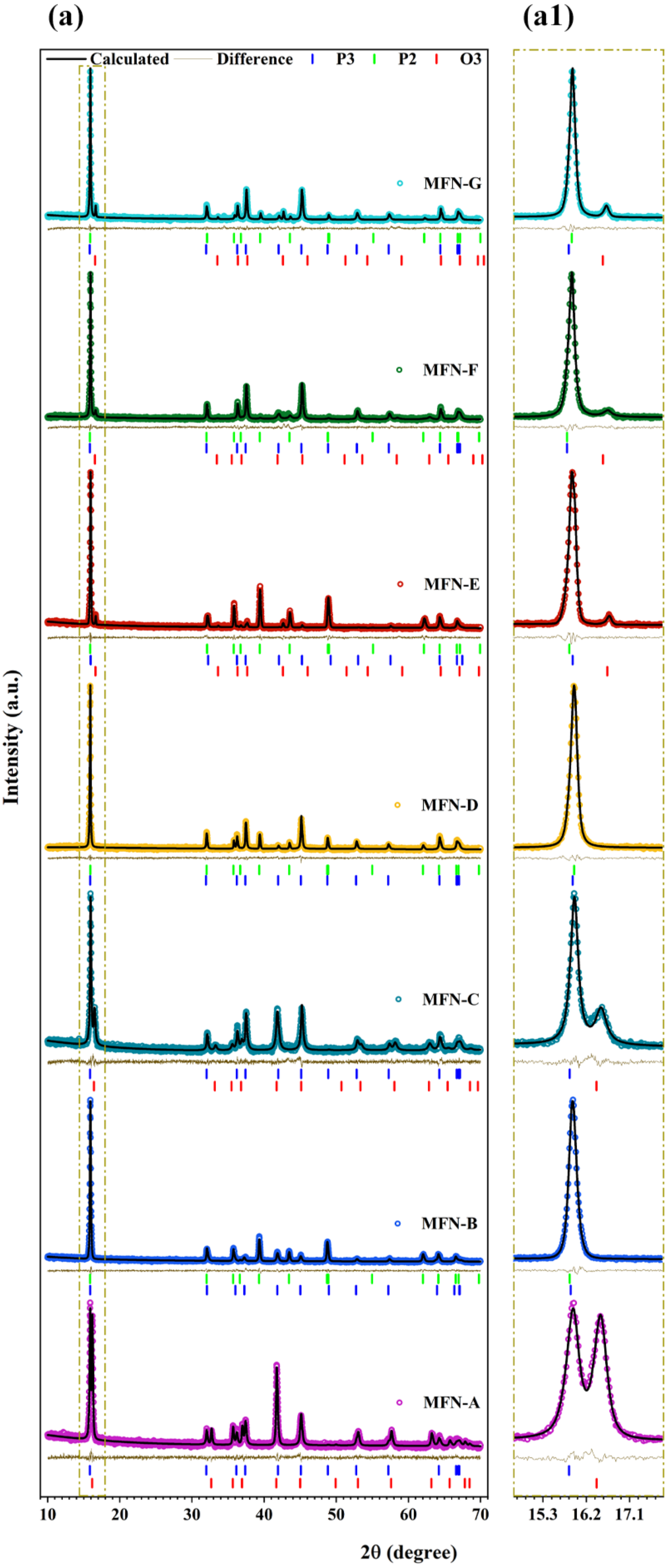

Fig. S5. (a) Rietveld refined patterns of MFN samples calcined at 700 °C, (a1) Magnified view of the most intense peak of P3, P2, and O3 phases.

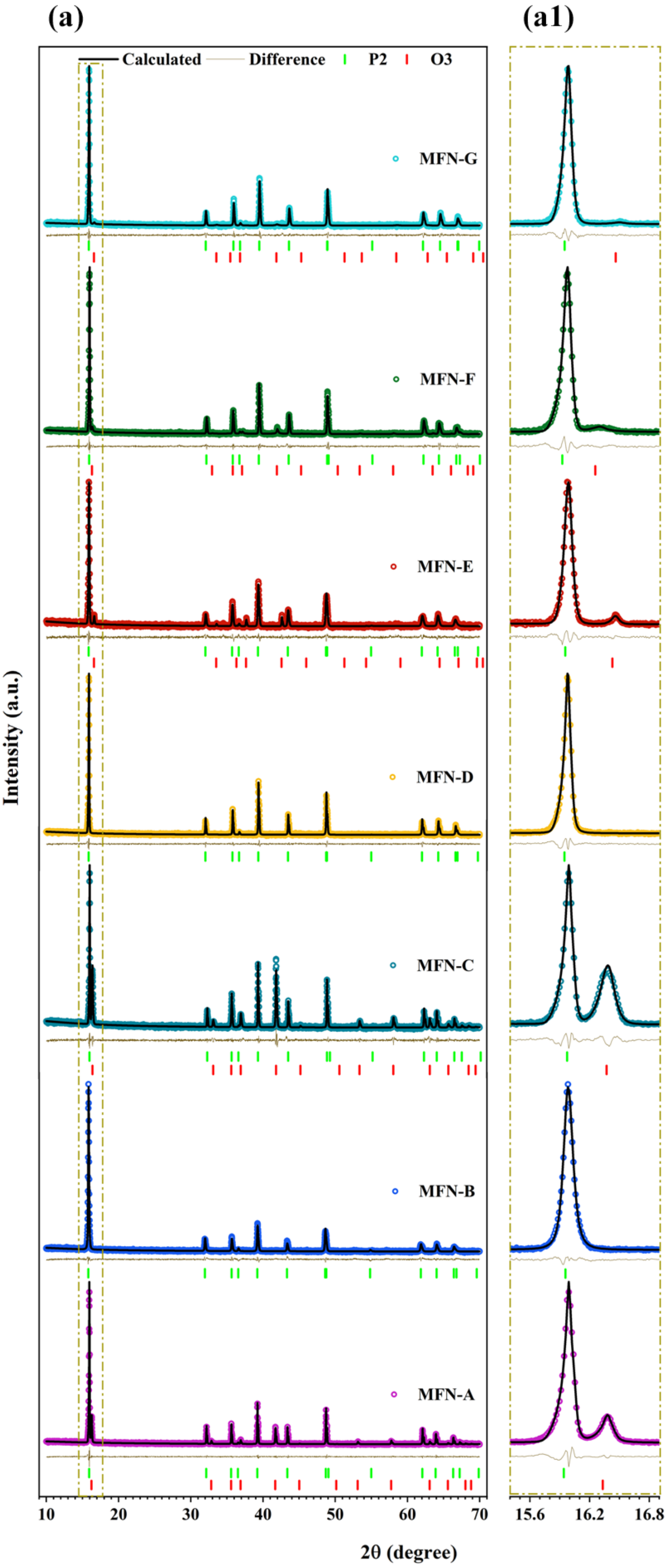

Fig. S6. (a) Rietveld refined patterns of MFN samples calcined at 900 °C, (a1) Magnified view of the most intense peak of P2 and O3 phases.

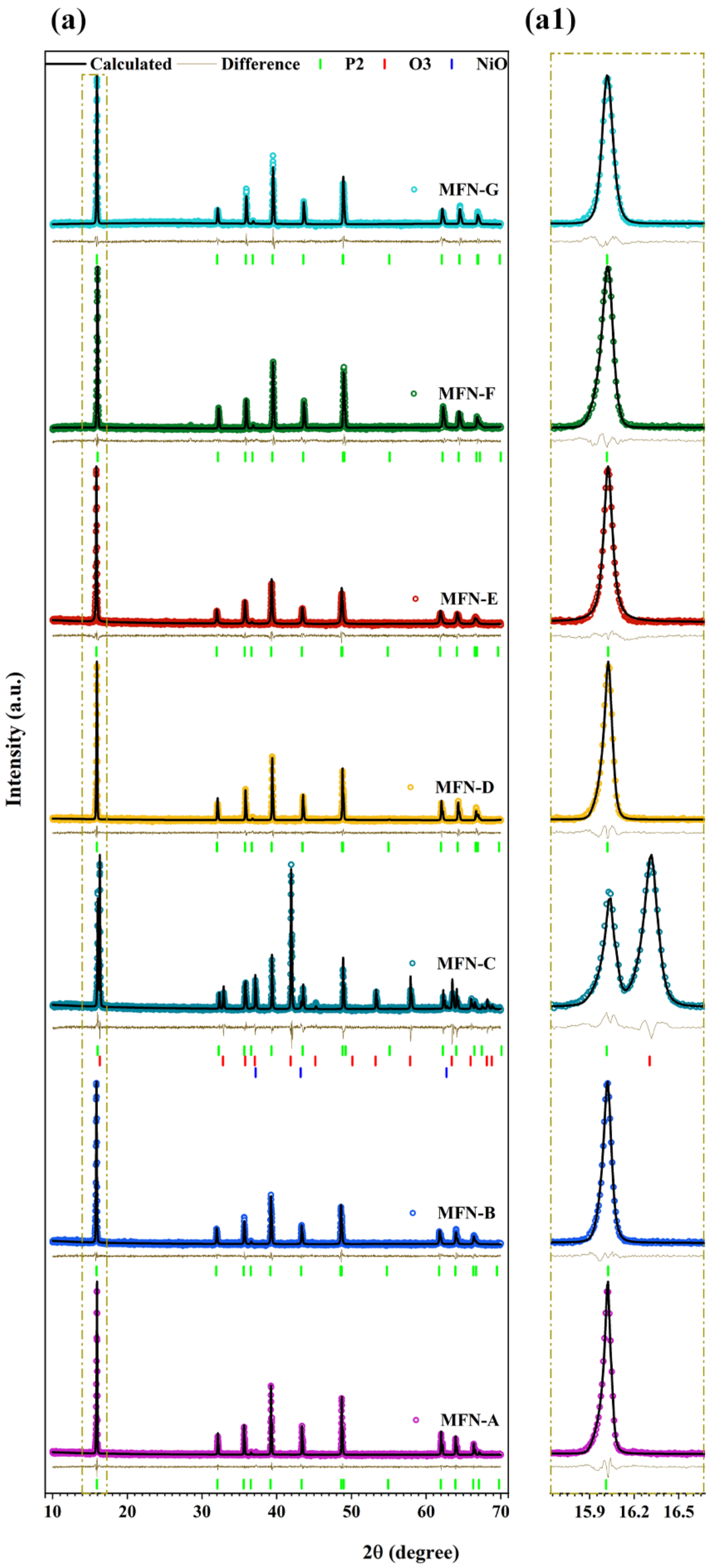

Fig. S7. (a) Rietveld refined patterns of MFN samples calcined at 1000 °C, (a1) Magnified view of the most intense peak of P2 and O3 phases.

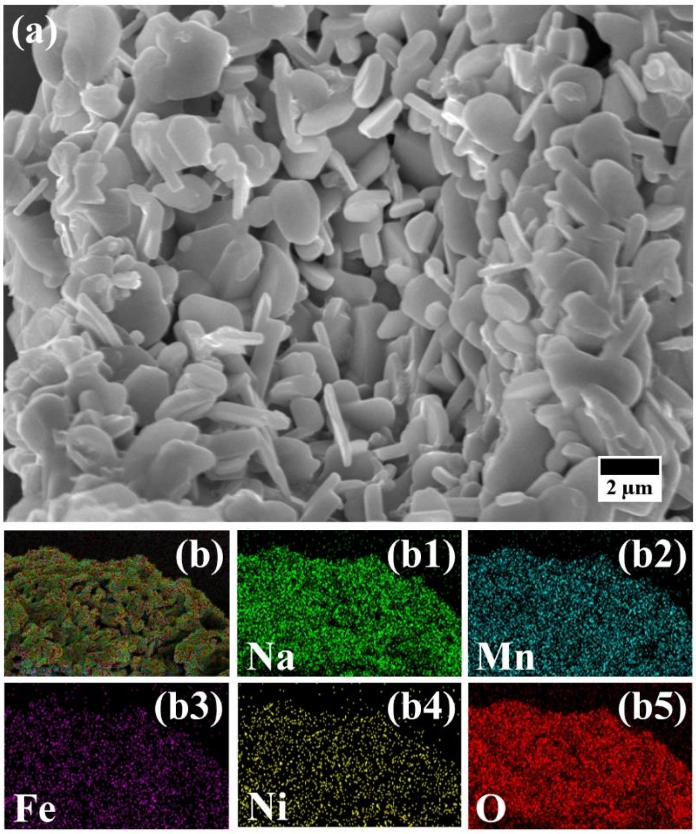

Fig. S8. (a) SEM micrograph of MFN-D sample calcined at 800°C. (b) EDS mapping indicating uniform distribution of constituent elements.

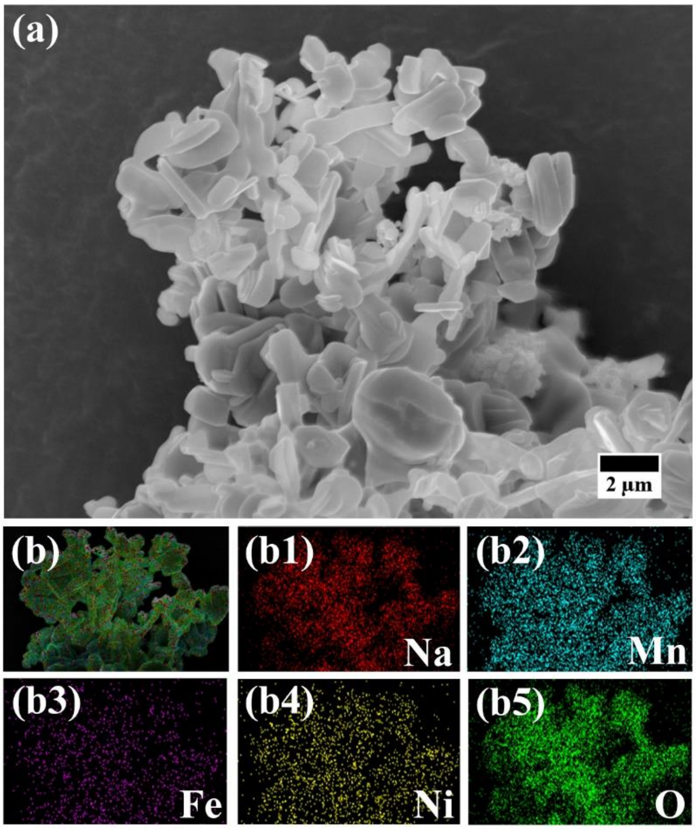

Fig. S9. (a) SEM micrograph of MFN-E sample calcined at 800°C. (b) EDS mapping indicating uniform distribution of constituent elements.

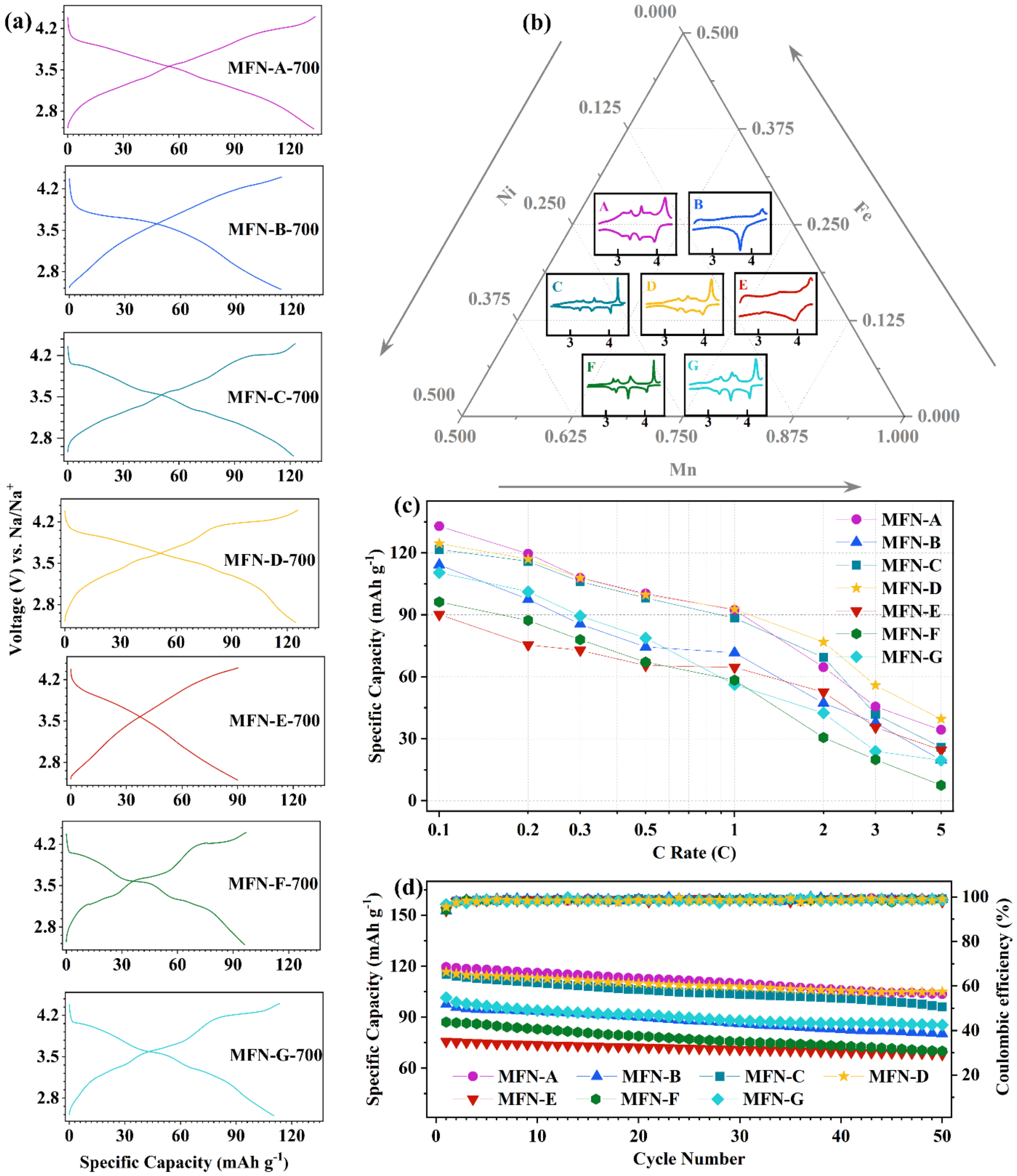

Fig. S10. (a) Galvanostatic charge-discharge curves at 0.1C, (b) dQ/dV vs. V profiles, (c) rate performance, and (d) cyclic stability of MFN samples calcined at 700℃.

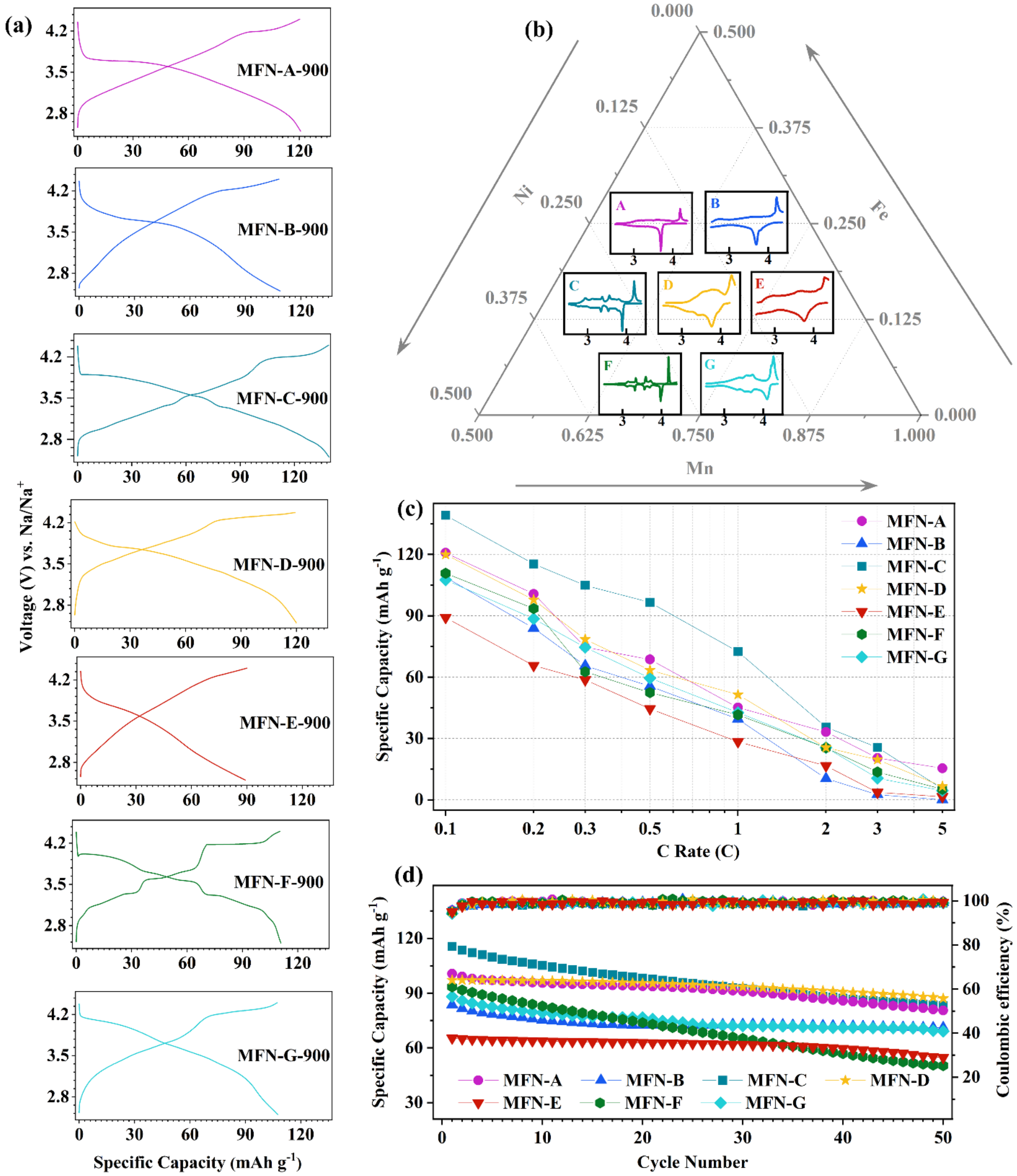

Fig. S11. (a) Galvanostatic charge-discharge curves at 0.1C, (b) dQ/dV vs. V profiles, (c) rate performance, and (d) cyclic stability of MFN samples calcined at 900°C.

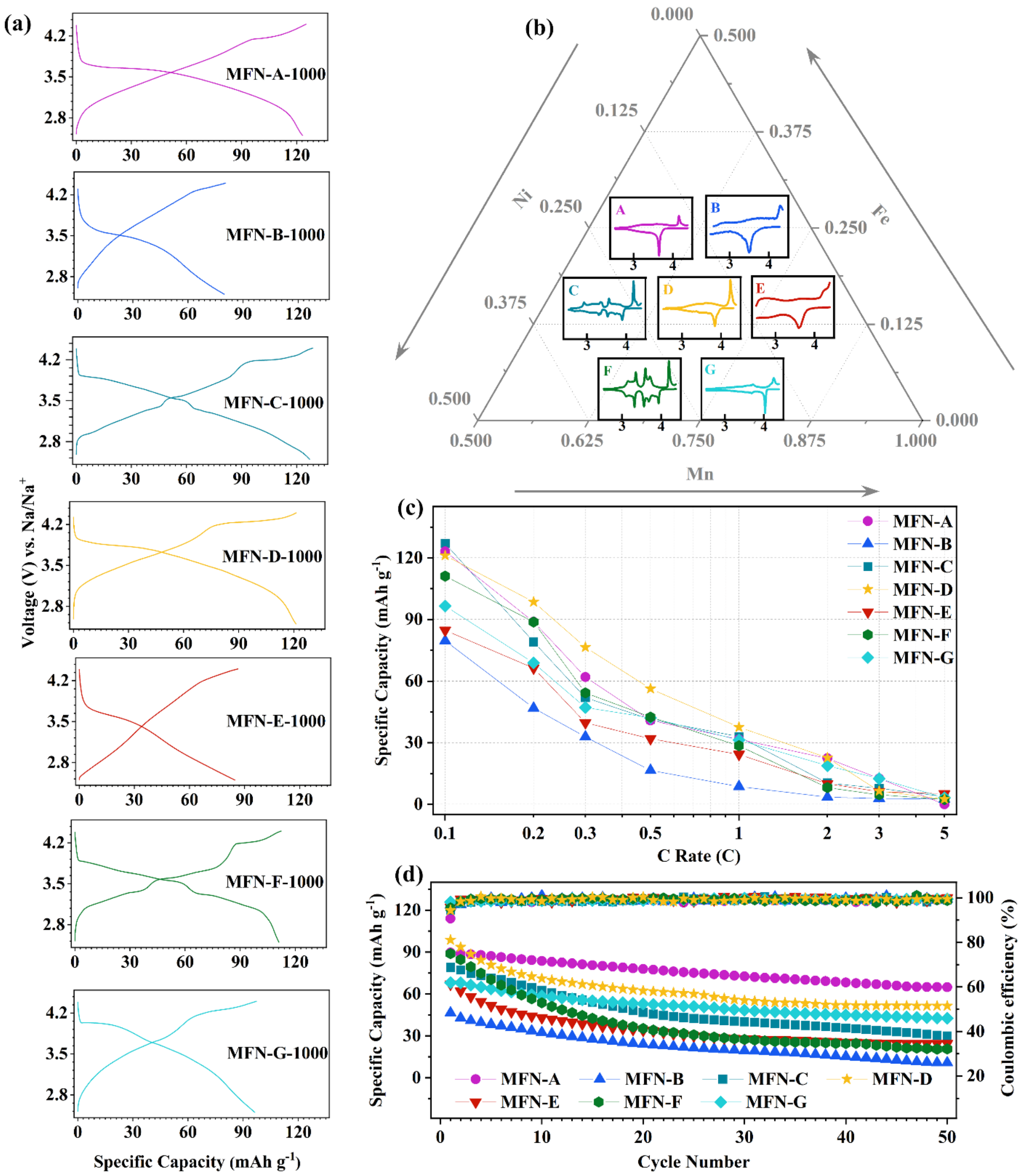

Fig. S12. (a) Galvanostatic charge-discharge curves at 0.1C, (b) dQ/dV vs. V profiles, (c) rate performance, and (d) cyclic stability of MFN samples calcined at 1000°C.

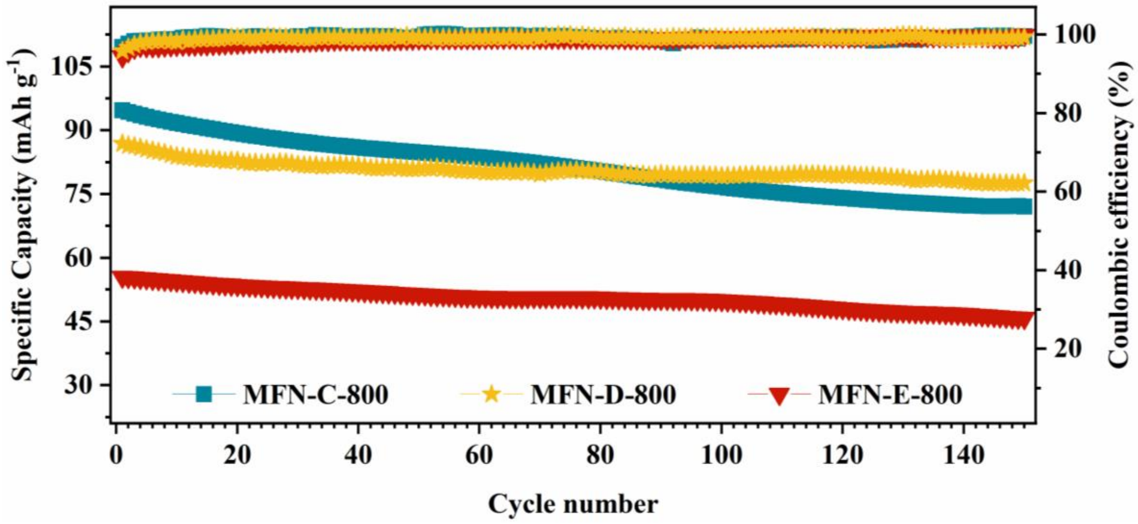

Fig. S13. Cyclic stability of MFN-C-800, MFN-D-800, and MFN-E-800 at 1C.

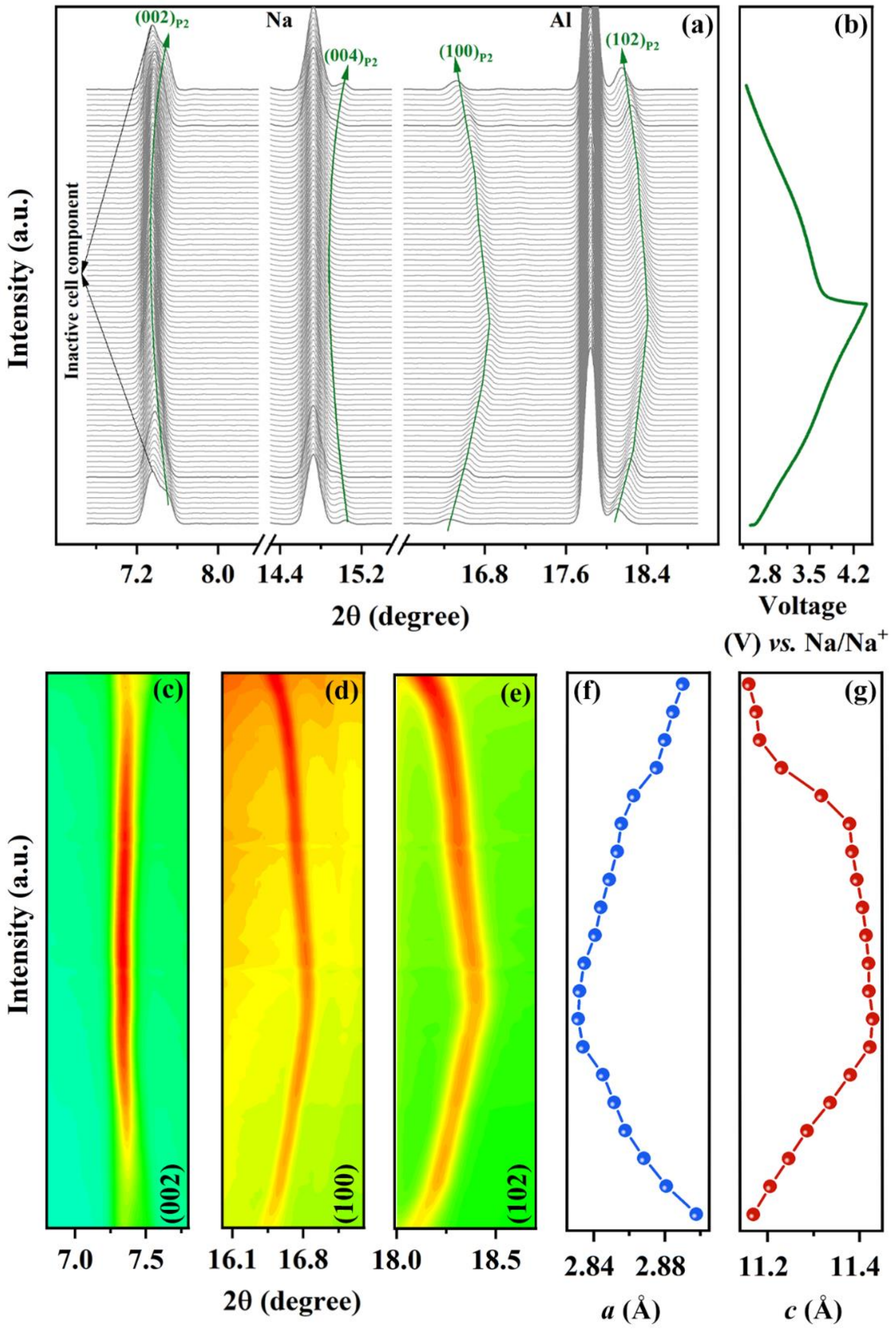

Fig. S14. (a) *Operando* synchrotron XRD patterns of MFN-E. (b) The corresponding GCD curve showing various states of charge/discharge. Color contour maps highlighting (c) (002), (d) (100), and (e) (102) peaks of the P2 phase of MFN-E. Variation in (f) *a* parameter and (g) *c* parameter of the P2 phase during charge/discharge.

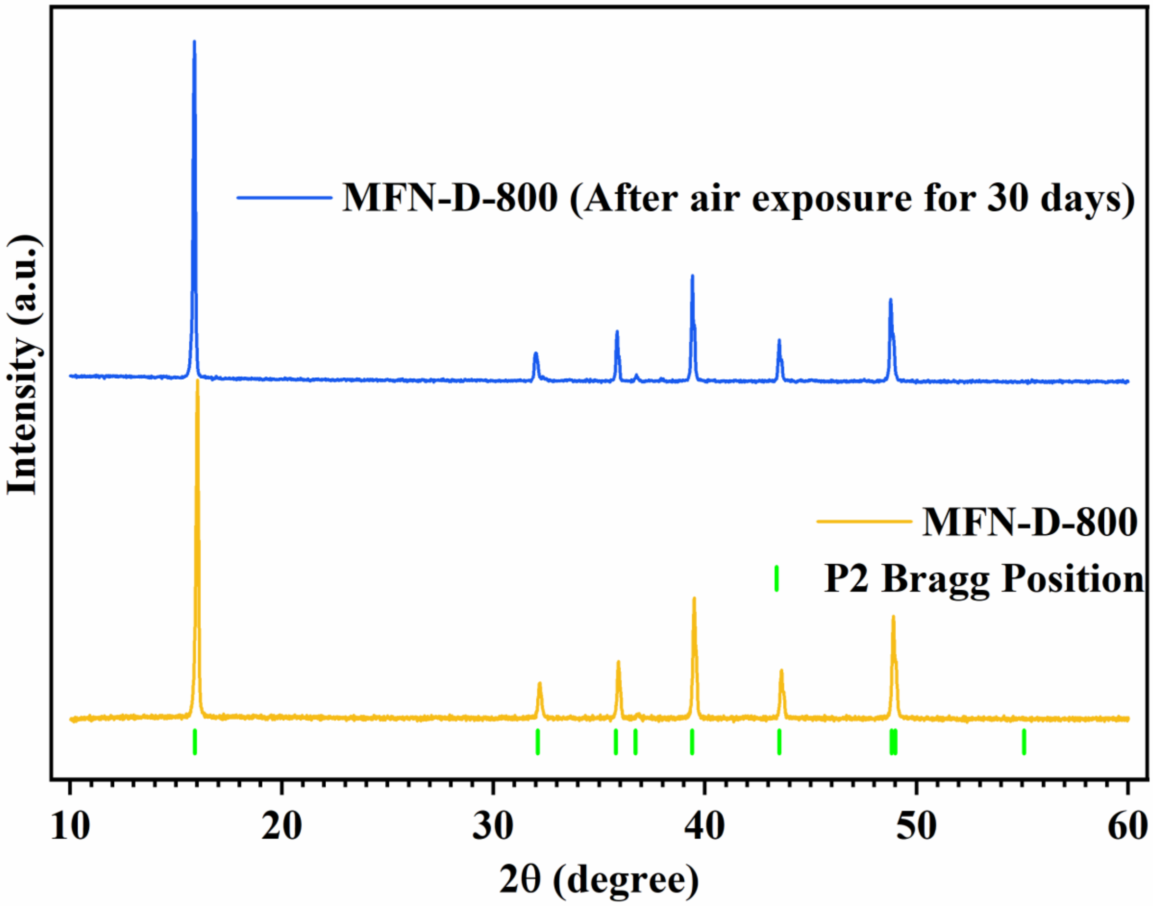

Fig. S15. XRD patterns of the MFN-D powder calcined at 800 °C before and after being exposed to air.

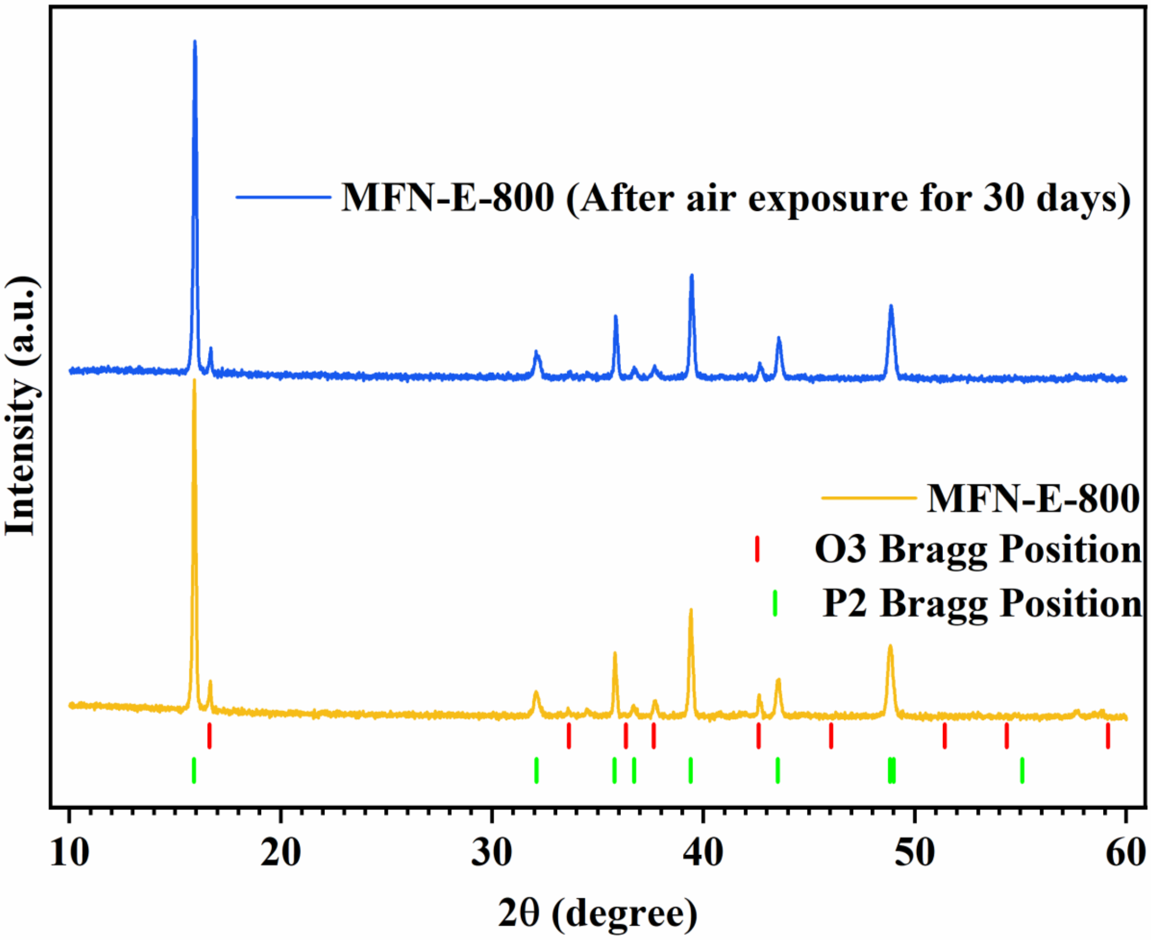

Fig. S16. XRD patterns of the MFN-E powder calcined at 800 °C before and after being exposed to air.

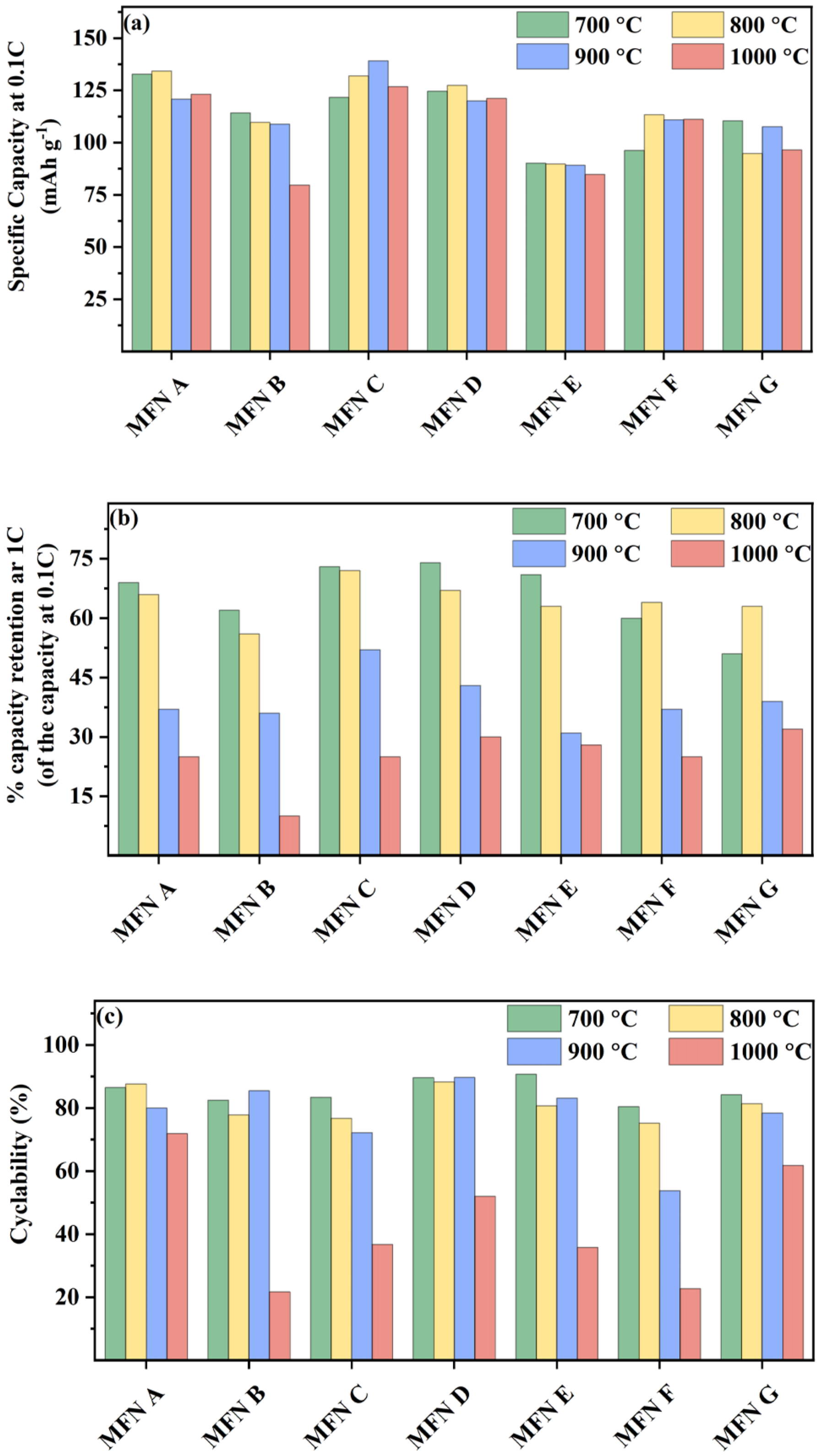

Fig. S17. Bar graphs comparing the (a) specific capacity, (b) rate performance, and (c) cyclability of various MFN cathodes at different calcination temperatures.

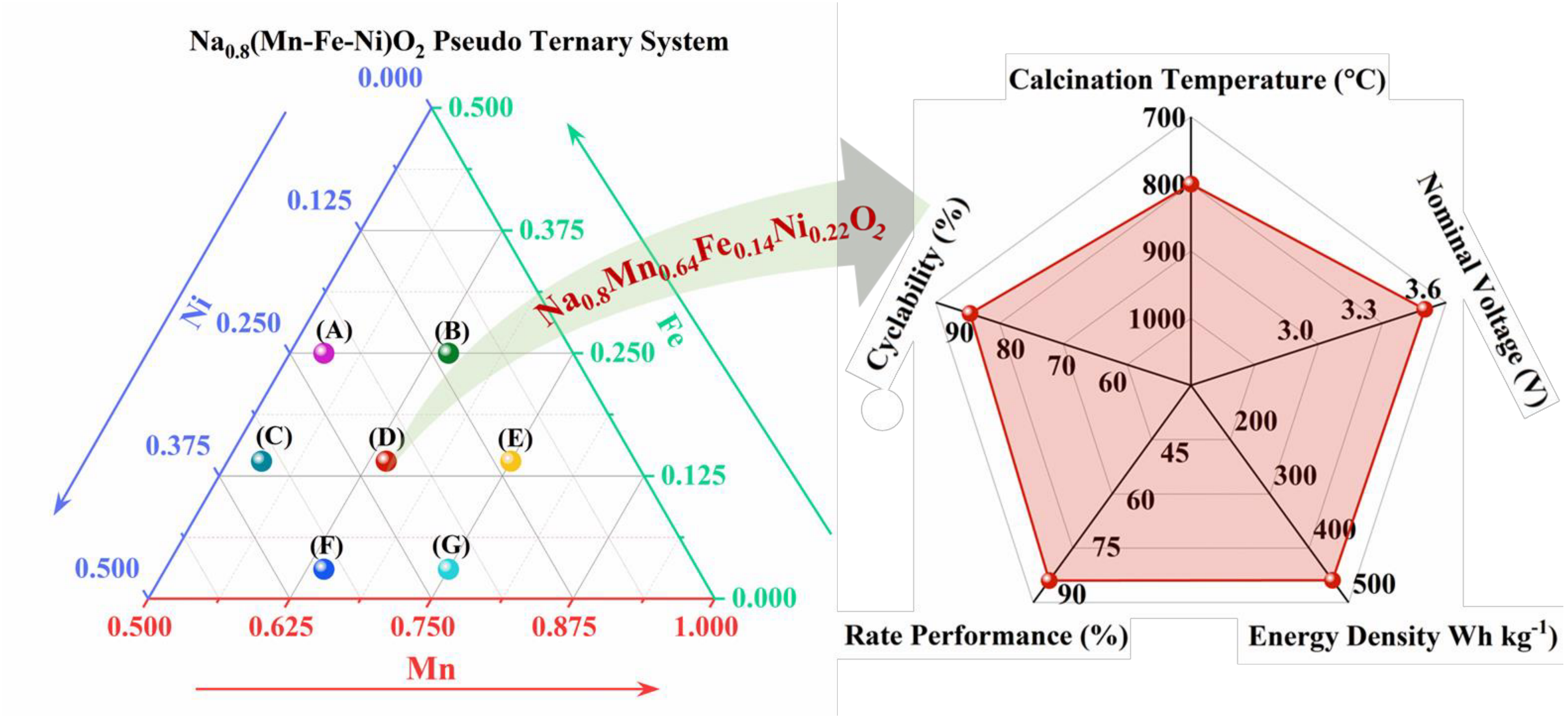
$Na_{0.8}(Mn\text{-}Fe\text{-}Ni)O_2$ Pseudo Ternary System
0.000
0.125
0.250
0.375
0.500
Ni
0.500
0.375
0.250
0.125
0.000
Fe
0.500
0.625
0.750
0.875
1.000
Mn
(A)
(B)
(C)
(D)
(E)
(F)
(G)
$Na_{0.8}Mn_{0.64}Fe_{0.14}Ni_{0.22}O_2$
Calcination Temperature (°C)
700
800
900
1000
Nominal Voltage (V)
3.6
3.3
3.0
Energy Density Wh kg^{-1})
200
300
400
500
Rate Performance (%)
45
60
75
90
Cyclability (%)
60
70
80
90